Ceramics International 52 (2026) 6301–6318

Contents lists available at ScienceDirect

Ceramics International

journal homepage: www.elsevier.com/locate/ceramint

Enhanced luminescence, photocatalytic and antibacterial performance of Ag^{+}/Eu^{3+} co-doped MgO nanophosphors

Remziye Tulek [a], Ali Teke [a], Guler Yagiz Erdemir [b], Orkun Babacan [c], Fatma Unal [d,e], Mustafa Burak Coban [a,f,*]

[a] Department of Physics, Faculty of Science and Letter, Balikesir University, Balikesir, Turkiye
[b] Department of Chemistry, Faculty of Science, Gazi University, Ankara, Turkiye
[c] Department of Veterinary, Kepsut Vocational School, Balıkesir University, Balikesir, Turkiye
[d] Department of Biomedical Engineering, Faculty of Engineering and Natural Sciences, Samsun University, Samsun, Turkiye
[e] Vocational School of Technical Sciences, Samsun University, Samsun, Turkiye
[f] Composite Research, Training and Simulation Application and Research Center, Balikesir University, Balikesir, Turkiye

ARTICLE INFO

Handling Editor: Dr P. Vincenzini

Keywords:
MgO:Ag^{+},Eu^{3+}
Co-precipitation
Luminescent
Photocatalytic degradation
Antibacterial effect

ABSTRACT

MgO, Ag-doped MgO, and Ag^{+}/Eu^{3+} co-doped MgO nanophosphors were synthesized by a co-precipitation method and systematically investigated for their structural, optical, antibacterial, and photocatalytic degradation properties. XRD confirmed the cubic MgO phase along with additional Eu_2O_3 and metallic Ag phases in co-doped samples, while SEM revealed a transition from irregular morphologies to spheroidized and layered agglomerated structures. Photoluminescence measurements showed strong red emission at 617 nm with maximum intensity at 2 wt% Eu^{3+}, followed by concentration quenching. Judd-Ofelt analysis revealed dominant electric-dipole transitions and low-symmetry Eu–O environments, confirming enhanced radiative probability and strong red emission, consistent with high color purity above 90 %, correlated color temperature in the warm light range (1746–2346 K), and excellent thermal stability with 83 % emission retention at 420 K. Antibacterial tests demonstrated selective inhibition of *Escherichia coli* but no activity against *Staphylococcus aureus*, with Ag enhancing and Eu^{3+} modulating the response. Photocatalytic degradation of crystal violet reached 83–84 % in doped samples compared to 75 % for pure MgO, with apparent pseudo-first-order rate constants more than twice that of undoped MgO, attributed to improved charge separation, where the synergistic roles of Ag^{+} (electron trapping) and Eu^{3+} (energy transfer) further promote reactive oxygen species generation and catalytic efficiency. These results establish Ag^{+}/Eu^{3+} co-doped MgO as a multifunctional material with promising applications in lighting, environmental remediation, and antibacterial systems.

1. Introduction

The increasing prevalence of antibiotic-resistant bacteria, together with the widespread contamination of aquatic systems by toxic organic pollutants, has created an urgent demand for advanced multifunctional materials capable of addressing both disinfection and environmental remediation challenges [1]. Metal oxide nanoparticles, with dimensions below 100 nm, exhibit unique physicochemical properties that make them highly suitable for such applications. Their broad-spectrum antibacterial activity, ability to interact extensively with cellular systems, stability under harsh environments and tunable structural and surface features highlight their potential as next-generation antimicrobial agents. Among these materials, nanostructured magnesium oxide (MgO) has attracted particular attention due to its strong antibacterial activity, high thermal stability, low cost, and excellent biocompatibility [2]. Recognized as safe for human use (FDA-approved), MgO nanoparticles combine low toxicity with high ionic character and abundant surface oxygen vacancies, enabling strong interactions with biological systems and pollutants [3,4]. These characteristics have expanded the applicability of MgO nanomaterials to diverse fields, including biosensing, adsorption, catalysis, agriculture, and nanofertilizers [5]. Importantly, MgO's antimicrobial efficacy and catalytic potential provide a unique platform for simultaneously eliminating pathogens and degrading hazardous compounds, thereby offering solutions to two critical global

* Corresponding author. Department of Physics, Faculty of Science and Letter, Balikesir University, Balikesir, Turkey.
E-mail address: burakcoban@balikesir.edu.tr (M.B. Coban).

https://doi.org/10.1016/j.ceramint.2025.12.387
Received 12 October 2025; Received in revised form 8 December 2025; Accepted 25 December 2025
Available online 25 December 2025

issues [4–6].

Pure MgO nanoparticles are inherently antibacterial, effectively inhibiting both Gram-negative *E. coli* and Gram-positive *S. Aureus* [7]. Their antibacterial action is primarily attributed to the generation of reactive oxygen species (ROS), which induce oxidative damage in microbial membranes, proteins, and DNA [2]. Additionally, MgO nanostructures such as nanorods have been reported to demonstrate superior catalytic activity under solar irradiation compared to commercial catalysts, further reinforcing their potential in environmental remediation [8]. This dual functionality has motivated their exploration as promising materials for water treatment applications, serving both to disinfect and to prevent biofilm formation.

Parallel to their antibacterial action, MgO nanoparticles exhibit intrinsic photocatalytic degradation activity. They can degrade organic dyes under UV light via electron-hole pair generation and ROS formation [8,9]. However, the wide band gap of MgO limits its activity to the UV range, which restricts photocatalytic degradation efficiency under solar irradiation. To overcome this limitation, metal ion doping has been employed as an effective strategy for tailoring the band structure and enhancing the catalytic and biological performance of MgO [10].

Silver doping has proven especially effective in this regard. Ag-doped MgO nanoparticles exhibit enhanced dye degradation efficiency, explained by the ability of Ag^+ ions to act as electron traps that suppress electron-hole recombination. Moreover, photoluminescence (PL) analyses indicate that Ag^+ incorporation quenches MgO defect-related emissions, directing charge carriers into chemical reactions rather than radiative recombination [11]. Beyond photocatalysis, Ag^+ also strengthens MgO's antibacterial activity. The synergistic effect of ROS generation by MgO and the bactericidal ion release from Ag^+ significantly improves antimicrobial performance [12]. Collectively, these findings establish Ag^+-MgO as a versatile nanomaterial with promising applications in both wastewater treatment and antimicrobial coatings [11,12].

While silver doping enhances the catalytic and antimicrobial capabilities of MgO, incorporating luminescent activators such as europium (Eu^{3+}) introduces valuable optical properties. Europium ions, with their sharp f-f transitions, can provide intense red luminescence in MgO matrices [13,14]. In some cases, Eu^{3+} doping has also led to broad white-light emission through combined Eu^{3+} transitions and host defect luminescence [15]. Such tunable luminescence expands potential applications to LED phosphors, bioimaging, optical probes, and security tagging. Additionally, given the inherent biocompatibility of MgO, the introduction of Eu^{3+} luminescence could enable the design of theranostic platforms that combine diagnostic imaging with therapeutic action.

Co-doping MgO with Ag^+ and Eu^{3+} brings together these complementary functionalities into a single multifunctional nanomaterial. While Ag^+ improves charge separation and antimicrobial properties, Eu^{3+} contributes luminescence and catalytic versatility. Importantly, the close proximity of Ag^+ nanoparticles to Eu^{3+} ions can generate plasmon-enhanced luminescence, intensifying Eu^{3+} emission through local surface plasmon resonance [16]. This synergistic effect has the potential to create nanostructures that are simultaneously antibacterial, photocatalytically active, and optically traceable, offering broad utility in wastewater treatment, biomedical coatings, and optoelectronic devices.

MgO is a wide-band-gap semiconductor (Eg ≈ 7 eV) [11,17], which limits its photoactivity to the UV region and leads to fast electron-hole recombination. Incorporating metal ions is an effective way to tune this electronic structure. Ag^+ introduces intermediate energy levels that trap electrons and suppress recombination, improving charge separation [11,18]. Eu^{3+} ions create localized states that further moderate recombination while providing characteristic luminescence [13–15]. Together, Ag^+ and Eu^{3+} enable a synergistic modification of MgO's recombination dynamics, enhancing its photocatalytic and optical performance.

Although Ag^+-doped MgO has been reported for photocatalytic and antibacterial applications and Eu^{3+}-doped oxide materials are known for their luminescent properties, fewer studies have addressed the combination of both functionalities within a single MgO system. In this work, Ag^+ and Eu^{3+} are jointly incorporated into MgO to develop a multifunctional material that simultaneously exhibits optical response, photocatalytic activity, and antibacterial behavior. In this context, the present study focuses on the synthesis and comprehensive characterization of MgO, Ag^+-doped MgO, and Ag^+/Eu^{3+} co-doped MgO nanophosphors prepared via a co-precipitation route. The primary aim is to elucidate how Ag^+ and Eu^{3+} incorporation influences the structural, optical, photocatalytic, and antibacterial performances of MgO.

2. Experimental details

2.1. Materials and methods of synthesis

2.1.1. Materials

Magnesium nitrate hexahydrate $Mg(NO_3)_2{\cdot}6H_2O$, silver nitrate ($AgNO_3$), $Eu(NO_3)_3{\cdot}5(H_2O)$ and citric acid monohydrate ($C_6H_8O_7{\cdot}H_2O$) were purchased from Sigma-Aldrich and used as precursors for the synthesis of undoped MgO, Ag-MgO and MgO: Eu^{3+}, 0.05Ag NPs. The preparation medium was double distilled water (DDW)

2.1.2. Synthesis of undoped MgO, Ag^+ doped MgO and Eu^{3+} and Ag^+ codoped MgO NPs

A systematic methodology forms the basis of the experimental procedures used to synthesize pure MgO phosphors and their doped samples, particularly MgO:Ag^+ and MgO:0.05Ag^+:Eu^{3+}. The precipitation method, which is simple and controllable, was employed for the production of undoped MgO phosphors. First, magnesium nitrate hexahydrate ($Mg(NO_3)_2{\cdot}6H_2O$, Sigma 99.9 %) was used as the starting material. In a series of careful steps, a 0.1 M $Mg(NO_3)_2{\cdot}6H_2O$ solution was prepared in 50 mL of distilled water, followed by the addition of a citric acid ($C_6H_8O_7H_2O$, 9 mmol) solution acting as a chelating agent. This solution was added dropwise to the reaction mixture while stirring continuously to prevent particle agglomeration. The next step of the process, aqueous ammonia (25 % by weight) was added dropwise to the mixture obtained at room temperature as a precipitating agent to carefully maintain the pH value at 10.5. The resulting suspension was stirred at a constant speed of 450 rpm for 4 h at 80 °C. The mixture was cooled to room temperature and then the suspension was aged for another 3 h at room temperature and purified by successive washing with slurry, distilled water, and ethanol. The material was then centrifuged at 4500 rpm for 10 min. It was then dried in an oven at 100 °C overnight. The material was then subjected to a process of fine grinding in an agate mortar and calcination at 450 °C for a period of 4 h. A similar systematic methodology was applied for the synthesis of MgO:0.05Ag^+ phosphors. In this case, a 0.1 M $Mg(NO_3)_2{\cdot}6H_2O$ solution was prepared by adding 0.05 wt percent Ag^+ ions from Ag^+ nitrate salt ($AgNO_3$, Sigma 99.9 %) to the solution, followed by the remaining steps similar to the production methodology of pure MgO phosphors. A parallel approach was adopted for the formation of MgO:0.05Ag^+,Eu^{3+}-doped phosphors. A 0.1 M Mg $(NO_3)_2{\cdot}6H_2O$ solution was prepared by dissolving Eu^{3+} ions in varying weight percentages (0.5, 1, 2, 3, 5, 7) of a 5 wt% Ag^+ and Eu^{3+} nitrate salt ($Eu(NO_3)_2{\cdot}5H_2O$, Sigma 99.9 %). The subsequent steps are consistent with the systematic approach previously described. This meticulous synthesis process employs precipitation methods and precise doping strategies to provide a foundation for a comprehensive investigation of the luminescent properties of the synthesized MgO phosphors and their potential applications. It should be noted that all NPs obtained were stored in a vacuum desiccator for subsequent analysis.

2.2. Characterization of NPs

FT-IR spectroscopy (Thermo Scientific Nicolet iS50) was used to

confirm the presence of functional groups and binding environments in the range of 4000–480 cm^{-1} at room temperature. PL spectra were measured using an ANDOR SR500i-BL luminescence spectrometer. This was equipped with a triple grating. It was also fitted with an intensified charge-coupled device (ICCD) camera. This was used as a detector for the visible region. The excitation source was a frequency-tripled Nd: YLFQ pulsed laser operating at 349 nm. X-ray diffraction (XRD) was employed to analyse phase composition and crystallinity using a Malvern Panalytical Empyrean diffractometer (Cu Kα, λ = 1.5406 Å). Data were collected over a 2θ range of 20–80°, with a step size of 0.02°. Surface morphology and microstructural characteristics were examined using a Zeiss scanning electron microscope (SEM) for compositional analysis.

2.3. Antibacterial activity

The antibacterial properties of the samples were evaluated against *Escherichia coli* and *Staphylococcus aureus* using the agar diffusion method, with bacterial strains obtained from the Culture Collection of the Department of Veterinary, Kepsut Vocational School, Balikesir University. Both bacteria were incubated in Nutrient Broth (Merck, Germany) at 37 °C for 24 h. After incubation, *E. coli* was cultured on MacConkey Agar (Merck, Germany) and *S. aureus* on Baird-Parker Agar, followed by incubation at 37 °C for 24 h. After incubation, colonies were subjected to Gram staining, oxidase, catalase, and coagulase tests, growth in TSI agar, and assessment of colony characteristics on the agar media to confirm purity [18]. Pure cultures of *E. coli* and *S. aureus* were then adjusted to 0.5 McFarland turbidity standard. The turbidity was verified using a spectrophotometer at 620 nm wavelength. To evaluate the antibacterial properties of the samples, each bacterium was separately inoculated onto the surface of Mueller Hinton Agar (Merck, Germany) using a sterile swab. The samples were then placed in disc form on the surface of the Mueller Hinton Agar and incubated at 37 °C for 24 h under aerobic conditions. The formation of a clear zone around the samples, indicating inhibition of bacterial growth, demonstrated the antibacterial activity of the samples. Samples that did not form an inhibition zone were considered to have no antibacterial effect against the tested bacteria [19].

2.4. Photocatalytic degradation

The photocatalytic activity of MgO, MgO:Ag^{+}, and MgO:Ag^{+},Eu^{3+} NPs was evaluated by monitoring the photocatalytic degradation of crystal violet (CV) dye under UV light. A 100 mL solution of CV with a concentration of $1x10^{-5}$ M was prepared, and 50 mg of the relevant NPs were added separately. Before the photocatalysis process, each NPs solution ($1x10^{-5}$ M CV + 50 mg NP) was stirred under a magnetic stirrer in the dark for 15 min. Then, each suspension was separately exposed to UV light with a wavelength of 254 nm and an intensity of 300 W, using a light source placed 30 cm away from the suspension surface. During the exposure period, approximately 2.0 mL suspension samples were taken every 15 min, and centrifugation was performed to separate the photocatalyst particles, followed by UV measurements. The excitation of the CV band at 590 nm was monitored.

3. Results and discussions

3.1. XRD analysis

Fig. 1 displays the XRD patterns of undoped and codoped MgO NPs. Measurements were carried out using a Malvern Panalytical Empyrean diffractometer with monochromatic CuK_{α} radiation (λ = 1.5406 Å), over the 2θ range of 20°–80° at a scan rate of 2°/min. For the undoped MgO NPs, diffraction peaks appeared at 36.91°, 42.88°, 62.21°, 74.66° and 78.55°, which correspond to the (111), (200), (220), (311)and (222) planes of the face-centered cubic MgO phase (space group *Fm-3m*, JCPDS #01-089-7746). In contrast, the Eu^{3+} and Ag^{+} codoped MgO NPs exhibit, in addition to the characteristic MgO reflections, new peaks arising from secondary Eu_2O_3 and metallic Ag phases. Reflections at 28.35° and 32.83° are indexed to the (111) and (200) planes of cubic Eu_2O_3 (bixbyite, space group *Ia-3*, JCPDS #00-032-0380), whereas peaks at 38.02°, 44.25°, 64.39° and 77.26° correspond to the (111), (200), (220) and (311) planes of metallic face-centered cubic Ag phase (space group *Fm-3m*, JCPDS #03-065-2871). Additional weaker reflections at 47.23° and 56.00° further support the presence of the Eu_2O_3 phase. These results clearly demonstrate that while the host MgO lattice is retained, Ag^{+} and Eu^{3+} incorporation through co-doping leads to the segregation of distinct Eu_2O_3 and Ag crystalline phases. The coexistence of these phases suggests limited solubility of Eu^{3+} and Ag^{+} ions in the

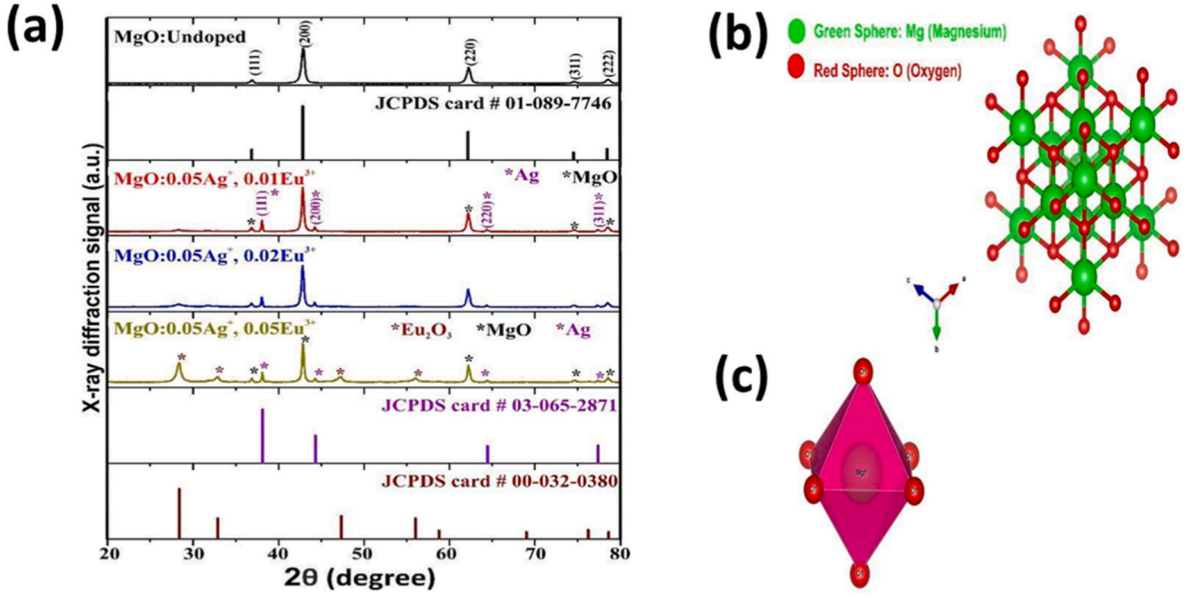

Fig. 1. (a) X-ray diffraction pattern of undoped MgO, MgO:Ag^{+} and MgO:0.05Ag^{+}:Eu^{3+} NPs, (b) schematic crystal structure of MgO illustrating cation distribution (c) polyhedral representations of Mg coordination environments in the MgO crystal structure, showing MgO_6 units.

MgO lattice under the applied synthesis conditions. Such phase evolution in co-doped MgO is consistent with previous report on noble metal-doped MgO systems, which also highlight the role of secondary phases in tailoring structural and functional properties [20].

3.2. FTIR analysis

To find functional groups, Fourier-transform infrared (FTIR) spectroscopy was used as an additional method in the phosphors characterization [21]. By performing FTIR characterizations, which is in the wave number range of 4000 to 480 cm^{-1}, the functional groups of the produced MgO, $MgOAg^{+}$, and $MgO:Ag^{+},Eu^{3+}$ NPs may be identified. Fig. 2 displays the FTIR spectrum of MgO, $MgOAg^{+}$, and $MgO:Ag^{+},Eu^{3+}$ NPs. They exhibit the stretching vibration mode, which indicates Mg–O–Mg bonds, ~652 and 858 cm^{-1}. The weak band, which indicates the bending vibration of the surface hydroxyl group, is seen at wave number around 1084 cm^{-1}. Although the band at 1084 was attributed -OH bending, the corresponding OH stretching band was not observed in the spectra. When Balakrishnan et al. used FTIR spectroscopy to study the MgO NP, they discovered a vibration mode in the 600–800 cm^{-1} wavenumber region, which indicated the presence of Mg–O–Mg bonds [22]. Similarly, Rohmawati et al. [23] reported that, in their study on MgO, they identified the characteristic peaks of MgO NP in the 950 cm^{-1}. Furthermore, OH stretching and bending bands were observed at approximately 3300 and 1400 cm^{-1}, respectively; these weak absorption bands may likely originate from surface adsorption processes during sample storage and can be attributed to MgO's sensitivity to H_2O and CO_2 [24].

3.3. Morphological properties: SEM analysis

The morphology and particle sizes of samples annealed at 450 °C for 4 h were examined using scanning electron microscopy (SEM). As shown in Fig. 3, the MgO structure appears irregular and randomly distributed. With the addition of $MgO:0.05Ag^{+}$, a tendency toward spheroidization is observed, along with the initiation of agglomeration at specific locations. This structural differentiation is attributed to the successful incorporation of Ag^{+} ions into the structure. Additionally, when the Ag^{+} and Eu^{3+} co-doping procedure was performed using the co-doping terminology with the host material MgO, it was observed that while the spheroidization trend continued, the agglomeration tendency formed a layered packing appearance in random and irregular positions. This suggests that the inclusion of Eu^{3+} ions in the main structure is responsible for the successful synthesis procedure.

3.4. Solid-state photoluminescence properties

PL emission spectra of $MgO:Eu^{3+}$ phosphors recorded at $\lambda_{exc} = 349$ nm are shown in Fig. 4. The photoluminescence (PL) emission spectrum, as shown in Fig. 4(a), exhibits characteristic peaks in the 500–750 nm wavelength range for $MgO:0.05Ag^{+}$, $0.02Eu^{3+}$ phosphor. Five distinct emission peaks are observed at 575, 595, 617, 652, and 705 nm. As shown in Fig. 4(b), the $MgO:0.05Ag^{+}$, $0.02Eu^{3+}$ sample exhibits two distinct features: a charge transfer band (CTB) in the ultraviolet (UV) region (220–280 nm) and a distinct, well-resolved spectral line in the near-ultraviolet (NUV) region (349 nm). The charge transfer band is fundamentally related to $O^{2-} \rightarrow Eu^{3+}$ CTBs arising from ligand-metal charge transfer between O_{2p} orbitals and the empty 4f states of Eu^{3+}. Such CTBs are traditionally accepted as a characteristic signature of Eu^{3+} in oxide host matrices, and it is widely accepted that their spectral positions shift depending on the covalent and coordination geometry of the host matrix. Furthermore, a distinct sharp line corresponding to intraconfigurational 4f–4f transitions has been identified; although parity is generally forbidden for free Eu^{3+} ions, it is partially allowed in solid-state environments due to the influence of the crystal field and single-parity phonon mixing. These narrow f–f spectral features serve as sensitive indicators of local symmetry and crystal field strength in Eu^{3+} sites and provide complementary data to that obtained from CTB [25]. Furthermore, the strongest peak at 617 nm corresponds to the $^5D_0 \rightarrow {}^7F_2$ transition in Eu^{3+} ions, while the peak values at 575, 595, 652, and 705 nm correspond to the $^5D_0 \rightarrow {}^7F_0$, $^5D_0 \rightarrow {}^7F_1$, $^5D_0 \rightarrow {}^7F_3$, and $^5D_0 \rightarrow {}^7F_4$ transitions, respectively (Fig. 4(b)) [26–29]. The highest luminescent intensity is exhibited by the orange-red luminescent band resulting from the $^5D_0 \rightarrow {}^7F_2$ transition among these luminescent bands. Fig. 4(c, d) shows the connection between the amount of Eu^{3+} that is added and how strong the light is at 617 nm in $MgO:0.05Ag^{+},xEu^{3+}$ (x = 0.005–0.07) phosphors. It is worth noting that the relative fluorescence intensity at 617 nm initially increases and then subsequently decreases. The optimum Eu^{3+} content is confirmed to be x = 0.02. More recently, Altowyan et al. [30] observed the threshold concentration of

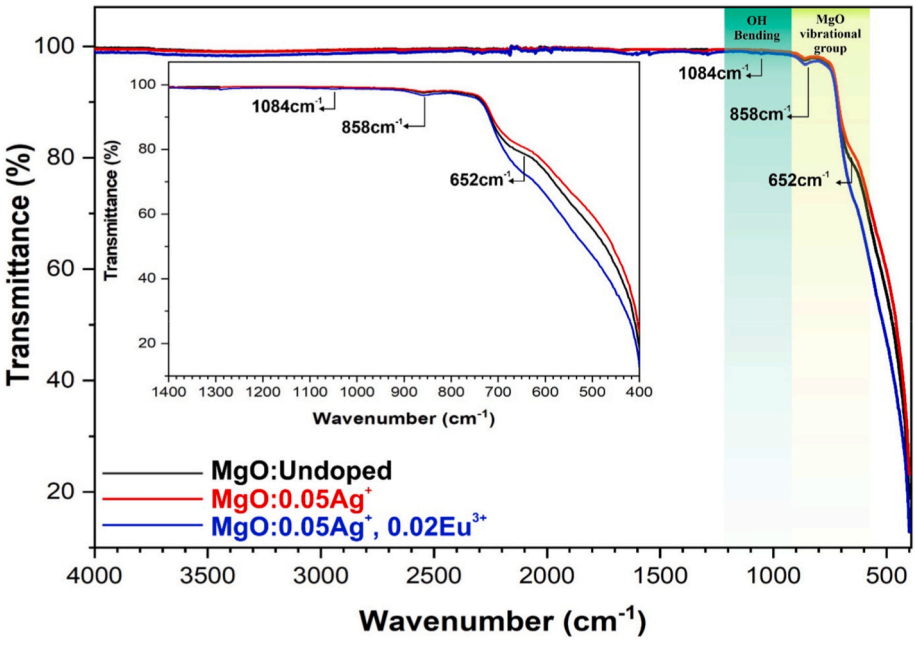

Fig. 2. FTIR spectrum of undoped MgO, $MgO:0.05Ag^{+}$ and $MgO:0.05Ag^{+},0.02Eu^{3+}$ NPs.

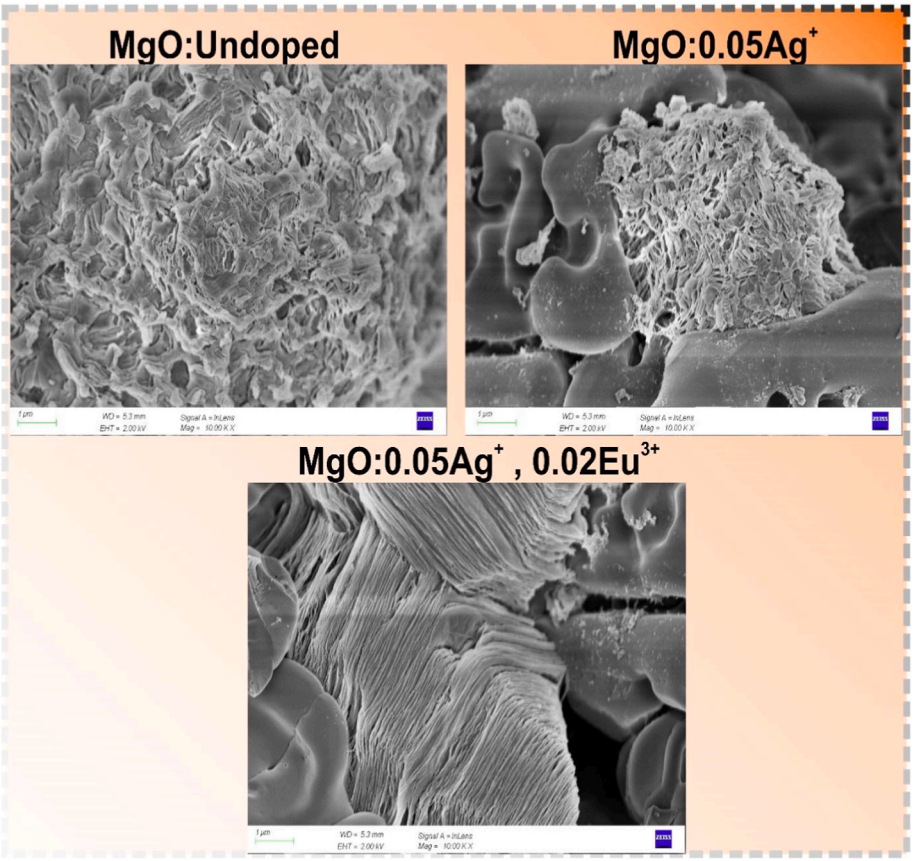

Fig. 3. SEM images of undoped MgO, MgO:0.05Ag^{+} and MgO:0.05Ag^{+}:0.02Eu^{3+} NPs.

Eu^{3+}-doped ZrO_2 phosphor samples as x = 0.02. Similarly, Kumar et al. [31] determined the critical dopant concentration of a $Y_2Si_2O_7$: Eu^{3+} nano phosphor sample as x = 0.03. At low concentrations, interactions between Eu^{3+} ions and the host lattice may be more significantly influenced by specific regions or defects, leading to a decrease in observed intensities. This phenomenon may arise from the greater influence of specific regions or defects on Eu^{3+} ion interactions at low concentrations.

Among these luminescent bands, the orange-red luminescent band resulting from the $^5D_0 \rightarrow {}^7F_2$ transition exhibits the highest luminosity, as shown in the inset figure in Fig. 4(d), which shows the concentration quenching graph of the prepared phosphors. The profile and position of the emission peaks remain unchanged as the dopant ion concentration rises, but the intensity of the peaks undergoes a substantial change. High concentrations of Eu^{3+} ions can cause concentration quenching, which is when the luminescence intensity weakens due to interactions between the Eu^{3+} ions. Fig. 4(c, d) shows the connection between the amount of Eu^{3+} that is added and how strong the light is at 617 nm in MgO:0.05Ag^{+},xEu^{3+} (x = 0.005–0.07) phosphors. Notably, the relative fluorescence intensity at 617 nm initially increases. Then it subsequently decreases. The optimum Eu^{3+} content is confirmed to be x = 0.02. When the concentration varies between 0.5 wt% and 2 wt%, the peak intensities increase and reach a maximum at 2 wt%. Once this threshold concentration is exceeded, quenching occurs according to the concentration quenching phenomenon as the distance between activator ions decreases. A similar observation has been reported by Lenczewska et al. [32]. Additionally, the average distance significantly facilitates energy transfer between dopant ions [30,33,34]. The PL intensity increased with the increase in Eu^{3+} concentration until reaching the threshold concentration value. This can be explained by the changes occurring in the immediate vicinity of Eu^{3+}. In addition to concentration-dependent effects, the presence of Ag^{+} nanoparticles may further enhance Eu^{3+} emission through plasmonic coupling. Ag^{+} nanoparticles exhibit localized surface plasmon resonance, which produces amplified local electromagnetic fields around neighboring Eu^{3+} ions. This plasmon-induced field can increase the probability of electric-dipole transitions, thereby further boosting the observed Eu^{3+} emission intensity. Similar plasmon-enhanced Eu^{3+} luminescence has been reported in previous studies [35,36].

3.4.1. *Concentration quenching phenomena*

Concentration quenching is a phenomenon that is typically influenced by factors such as exchange interaction, multipole-multipole interaction, or radiation reabsorption [37]. Concentration quenching is generally attributed to energy transfer between adjacent Eu^{3+} ions. To better comprehend the concentration quenching effect that is observed in Eu^{3+}-doped MgO, it is necessary to calculate the critical distance (R_c) between the two activator ions (donor and acceptor). This calculation is critical for determining the specific mode in which the energy is transferred. To understand the complex dynamics that are involved in the energy transfer between Eu^{3+} ions in the MgO matrix, the Blasse formula [38] is used to calculate the critical distance (R_c): MgO: To better understand the quenching mechanism of Eu^{3+} phosphors, Blasse's theory, which states that energy transfer is primarily influenced by exchange interactions when the distance between two luminescent centers is less than 5 Å, can be applied. Beyond this threshold, electric multipole interactions become the dominant factors. The distance separating Eu^{3+} ions can be approximately calculated using the Blasse formula [38]:

$$R_c \approx 2\left[\frac{3V}{4\pi x_c N}\right]^{\frac{1}{3}}$$

where x_c and N are defined as functions of the parent lattice structure and dopant concentration. N is a measure of the degree of doping. It is

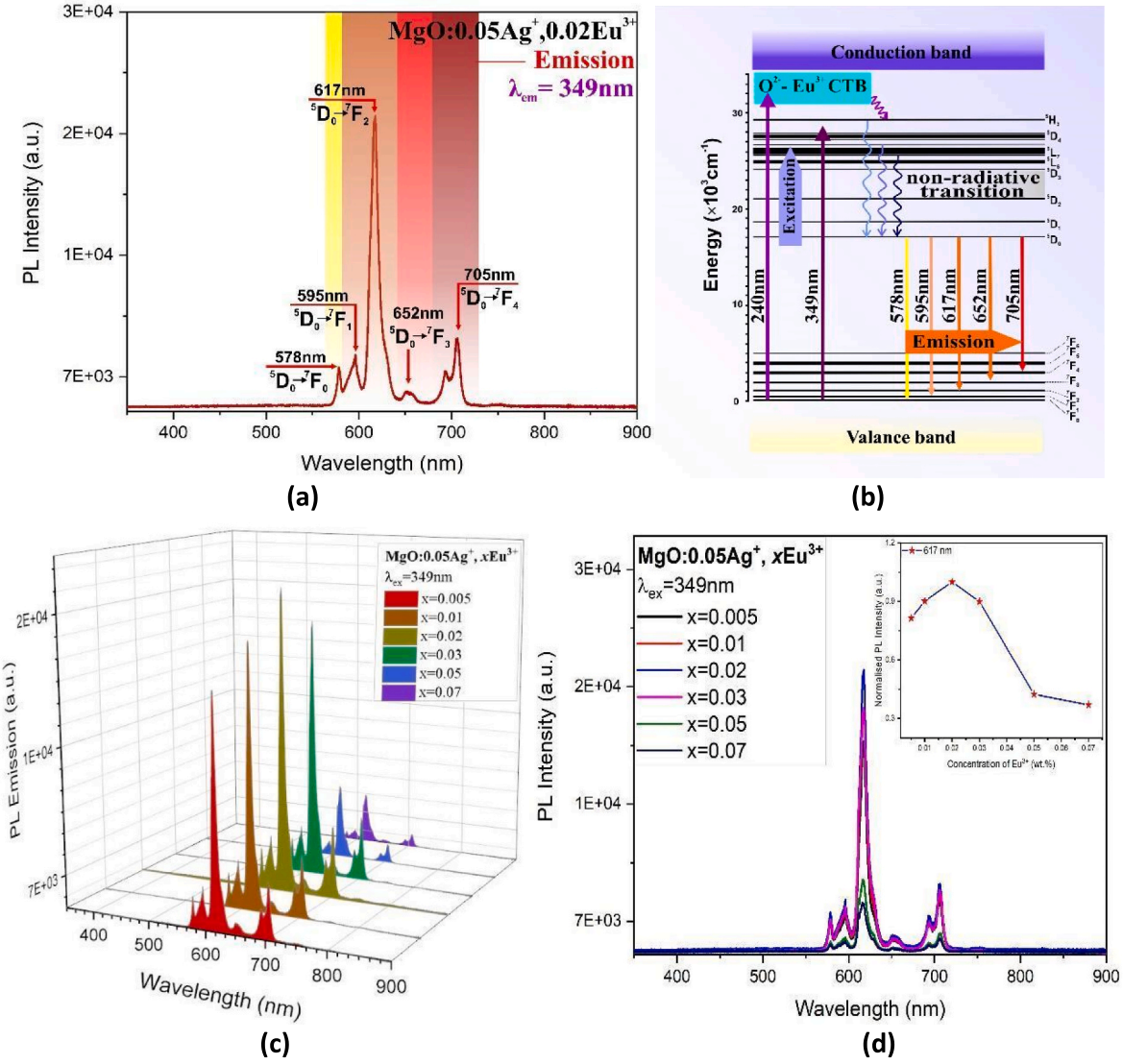

Fig. 4. (a) 2D emission spectrum of MgO:Ag^{+},0.02Eu^{3+} phosphor with possible electronic transitions. (b) Schematic representation of the excitation and emission processes in Eu^{3+}-activated MgO:0.05Ag^{+} The energy level diagram of Eu^{3+} shows the key excitation wavelengths and corresponding radiative transitions.(c) 3D PL emission spectra of MgO:0.05Ag^{+} co-doped with varying concentrations of Eu^{3+} under 349 nm excitation.(d) 2D PL emission profile of MgO:0.05Ag^{+} doped with Eu^{3+} at various concentrations. The inset figure shows normalized PL intensities and concentration quenching behavior for the $^{5}D_{0}\rightarrow{}^{7}F_{2}$ ED transition (617 nm).

used to calculate the level of electronic excitation. *V* is a measure of the crystal volume and is used to estimate its internal luminosity. V is equal to 75.0 $Å^{3}$, x_c is equal to 0.02 and N is equal to 4. The critical distance (R_c) analyzed for Eu^{3+} is approximately 12.145 Å, which is significantly larger than 5 Å. It follows that the energy transfer mode, exchange interactions and radiation absorption are all the result of electrical multipolar interactions. This indicates that Eu^{3+} is a highly efficient energy donor for luminescence, which is a process that involves the emission of light. Furthermore, when Eu^{3+} is positioned close to a luminescence centre, the efficiency of energy transfer increases. This makes Eu^{3+} an important luminescent material. It is useful for many photonic applications. Electrical multipole interactions can be divided into three types. The first type is dipole-dipole (d-d). The second type is quadrupole-quadrupole (q-q). The third type is dipole-quadrupole (d-q). [39]. To define a specific type of electrical multipole interaction, the following equation, derived from Dexter's theory [40], is generally applied to verify the type of electrical multipole interaction in Eu^{3+} ions:

$$\frac{I}{x}=K\left(1+\beta(x)^{\frac{Q}{3}}\right)^{-1}$$

where I indicates the luminescence intensity and x indicates the Eu^{3+} doping concentration. Under the same matrix conditions and consistent test parameters, both *K* and β behave as constants. The values 6, 8, and 10 correspond to dipole-dipole, dipole-quadrupole, and quadrupole-quadrupole interactions, respectively. Fig. 5 shows the linear correlation between *log(I/x)* and *log(x)*. According to Dexter's resonance energy transfer theory, the obtained -*Q*/3 slope is calculated as −2.64. As a result, the derived value of *q* is calculated as 7.92, which is the value closest to 8, indicating that the primary mechanism of the quenching of MgO:Eu^{3+} phosphor is energy transfer caused by dipole-quadrupole (d-q) interactions between Eu^{3+} ions.

To investigate the Eu^{3+} photoluminescence dynamics in more detail, time-resolved decay profiles were recorded for the selected compositions as shown in Fig. 6. The decay profiles measured for the $^{5}D_{0}$ transition were examined for the MgO matrix and MgO:0.05Ag^{+} composition with 0.02Eu^{3+} doping. MgO and MgO:0.05Ag^{+},0.02Eu^{3+} phosphors were obtained by measuring emission at 617 nm and excitation at 349 nm. The luminescence decay curves show good agreement with a double exponential function.

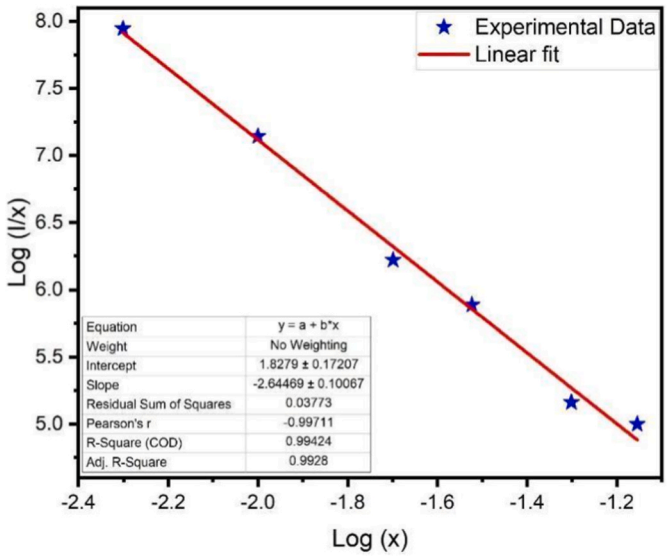

Fig. 5. Log (I/x) vs log x plot (Dexter plot).

$$I_t = I_0 + A_1 e^{-\frac{t}{\tau_1}} + A_2 e^{-\frac{t}{\tau_2}} \quad (1)$$

The average lifetime of the phosphors was calculated using the following equation (2)

$$\tau_{avg} = \frac{A_1\tau_1^2 + A_2\tau_2^2}{A_1\tau_1 + A_2\tau_2} \quad (2)$$

where 'I_t' and 'I_0' are the emission intensities at times 't' and '0', respectively. 'A_1' and 'A_2' are constants. 'τ_1' and 'τ_2' are the decay times of the double exponential function. It has been observed that the concentration of the additive affects the lifetime. The MgO matrix without additives exhibits relatively fast and weak decay (τ_{avg} = 1.060 ms), indicating that radiative processes are negligible. When MgO:0.05Ag^{+}, 0.02Eu^{3+} is added, a significant increase in the decay lifetime is observed (τ_{avg} = 1.522 ms), indicating the activation of radiative pathways associated with Eu^{3+}. It has been confirmed by the calculated values that the prepared phosphor materials are suitable for solid-state lighting applications.

3.4.2. Judd-Ofelt theory

Judd-Ofelt (JO) Analysis is a theoretical calculation that is used to predict the spectral characteristics and site symmetry of rare earth ions in different host matrices. This analysis is a very useful tool for predicting two types of parameters: density parameters and radiation parameters. It also provides information about the local symmetry and valences of the surrounding ligands [41,42]. It uses three basic parameters to describe the optical behavior of these ions. Density parameters obtained from emission spectra, Ω_J (J = 2, 4, 6), and dipole strength parameters Ω (Ω_2, Ω_4, Ω_6), determine the local symmetry and nature of the environment surrounding rare earth ions, while radiation parameters are derived from the Ω parameters [43]. The Ω_2 parameter depends on the local symmetry of the ligand field and the intensity of the covalent bond [44]. In highly symmetric environments, rare earth ions tend to have low Ω_2 values, whereas this value increases when the intensity of the covalent bond increases and the local symmetry of the ligand field decreases. The electronic levels of free ions are lowered by covalent bonding, leading to an increase in Ω_2 values. The understanding of Ω_4 and Ω_6 is less clear, although they are related to the viscosity of the host medium containing the ions, the packing density of the lattice, and the hardness surrounding the rare earth ion [45]. Vibronic interactions between the rare earth ion and the ligand can alter Ω_4 and Ω_6. By determining these parameters, oscillator strengths, branching ratios, excited state radiative lifetimes, and energy transfer probabilities can be calculated.

3.4.3. The JO intensity parameters and radiative analysis

For Eu^{3+} ions, the density parameters Ω_2 and Ω_4 were calculated using the following equation based on the integrated emission intensities of the $^5D_0 \rightarrow {}^7F_J$ transitions (J = 2, 4).

$$\Omega_J = \frac{S_{MD}(\vartheta_1^3)}{e^2(\vartheta_J^3)} \frac{9n^3}{n(n^2+2)^2} \frac{\int I_1 \vartheta_1}{|\langle J\|U^J\|J'\rangle|^2 \int I_J \vartheta_J} \quad (3)$$

where I_1 and I_J are the integrated intensities of the $^5D_0 \rightarrow {}^7F_1$ and $^5D_0 \rightarrow {}^7F_J$ transitions, respectively, ϑ is the transition frequency, S_{MD} = 9.6×10^{-42} (esu^2cm^2) is the magnetic dipole line strength ($^5D_0 \rightarrow {}^7F_1$), e = 4.803×10^{-10} (esu) is the elementary charge, n is the refractive index,

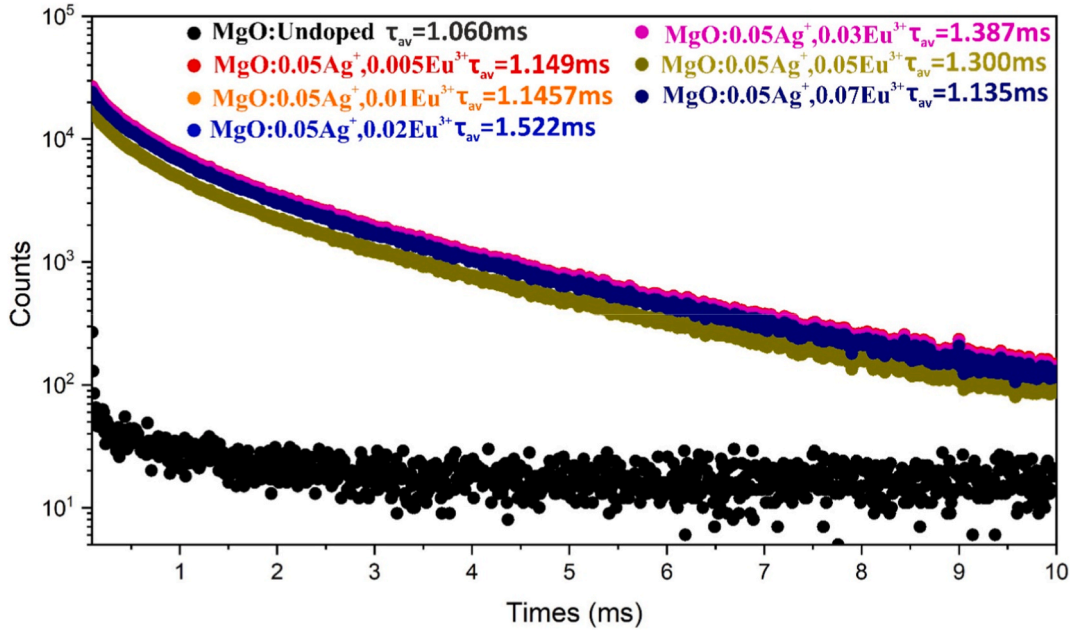

Fig. 6. Lifetime curve of undoped MgO and MgO:0.05Ag^{+},xEu^{3+} (x = 0.00–0.07) phosphor.

ϑ is wavenumber of transition and $\left|\langle J\|U^J\|J'\rangle\right|^2$ are the unitary matrix elements. *The refractive index of the samples can be calculated from the band range value using the Dimitrov and Sakka correlation* [46].

$$\frac{(n^2-1)}{(n^2+2)}=1-\sqrt{\frac{E_g}{20}} \tag{4}$$

where n is a refractive index (estimated as n 1.72210). The optical band gap of MgO was taken from the literature (Eg = 7.30 eV) [47]. $\|U^{\lambda}\|^2$ (λ = 2, 4 and 6) are calculated squared matrix elements taken from Verma et al., which is given in Table 1 [48].

In this study, Ω_6 parameters cannot be determined due to the absence of the $^5D_0 \rightarrow {}^7F_6$ transition in photoluminescent spectra. As a result, only the $^5D_0 \rightarrow {}^7F_J$ (J = 1, 2, 4) transitions are used to calculate the radiative transition probabilities. The probabilities of spontaneous radiative transitions A(J, J′) can be calculated by combining Eq. (5) and Eg. (6) equations using the following Eq. (7) [49–51].:

$$A_{01}^{MD}=\frac{64\pi^4\vartheta^3}{3h(2J+1)}\times\chi_{MD}\times S_{MD} \tag{5}$$

$$A_{0J}^{ED}=\frac{64\pi^4\vartheta^3}{3h(2J+1)}\times\chi_{ED}\times S_{ED} \tag{6}$$

$$A(J,J')=\frac{64\pi^4\vartheta^3}{3h(2J+1)}[\chi_{ED}\times S_{ED}+\chi_{MD}\times S_{MD}] \tag{7}$$

where, n is the refractive index, h is the Planck constant, $(2J + 1)$ is the degeneracy of the initial state, and the local field corrections χ_{ED} and χ_{MD} for the ED and MD transitions are defined in Eqs. (8) and (9), respectively, using the refractive index. S_{ED} and S_{MD} are the electric dipole and magnetic dipole line strengths (esu^2 × cm^2). The electric dipole line strength (S_{ED}) related to the JO parameters can be found using Eq. (10) [52].

$$\chi_{ED}=\frac{n(n^2+2)^2}{9} \tag{8}$$

$$\chi_{MD}=n^3 \tag{9}$$

$$S_{ED}=e^2\sum_{J=2,4,6}\Omega_J\left|\langle J\|U^J\|J'\rangle\right|^2 \tag{10}$$

By combining Eq. (4) and Eq. (5), the asymmetry ratio R can be derived from ED and MD as follows Equation (11) [53]:

$$R=\frac{A_{ED}\left({}^5D_0\rightarrow{}^7F_{2,4,6}\right)}{A_{MD}\left({}^5D_0\rightarrow{}^7F_1\right)}=\left[\frac{\vartheta_J}{\vartheta_{MD}}\right]^3\times\frac{S_{ED}}{S_{MD}}\times\frac{\chi_{ED}}{\chi_{MD}} \tag{11}$$

The asymmetric ratio R can be calculated directly from the PL emission spectra by calculating the integrated intensity ratio of the transitions ED ($^5D_0 \rightarrow {}^7F_{2,4}$) and MD ($^5D_0 \rightarrow {}^7F_1$) and can be expressed as follows (Eq. (12)) [54,55]:

$$R=\frac{\int I_{ED}d\vartheta}{\int I_{MD}d\vartheta} \tag{12}$$

The findings obtained using the J-O concept are shown in Table 2. The ligand environment is directly related to the JO characteristic parameter Ω_2 (associated with the short-range effect), which reveals the lack of symmetry of Eu^{3+} ions. On the other hand, the other parameter Ω_4 (related to the long-range effect) is significantly influenced by volumetric properties such as the hardness of the main phosphor's brightness and is not affected by the surrounding environment. The density parameter Ω_6, associated with the $^5D_0 \rightarrow {}^7F_6$ transition in the infrared region, was not investigated in this study as it was not observed in the current work. According to the calculated value, the density parameter of the $^5D_0 \rightarrow {}^7F_2$ transition is dependent on the Eu^{3+} ion concentration. As summarized in Tables 2 and in the MgO:0.05Ag^+,Eu^{3+} series, as the Eu^{3+} concentration increased from 0.005 to 0.07, the Ω_2 and Ω_4 parameters increased from 7.99 to 9.23 × 10^{-20} cm^2 and from 3.34 to 3.42 × 10^{-20} cm^2, respectively. Additionally, the $^5D_0 \rightarrow {}^7F_2$ (Ω_2) density parameter value is higher than the $^5D_0 \rightarrow {}^7F_4$ (Ω_4) value for all samples. This $\Omega_2 > \Omega_4$ trend is well-supported in the literature [52]. High Ω_2 and Ω_4 values indicate that dopant ions occupy lower symmetry regions and cause greater local distortion in Eu–O bonds. Such distortions not only support electric dipole transitions but are also attributed to the more covalent character of Eu–O bonds at high dopant levels. An important feature of photoluminescence is the asymmetric ratio associated with emission tuning. The ratio of the integral densities of electric ($^5D_0 \rightarrow {}^7F_2$) and magnetic ($^5D_0 \rightarrow {}^7F_1$) dipole transitions is known as the asymmetric ratio. The asymmetric ratio provides a more detailed assessment of the deformation of the nearest environment's inversion region in relation to the symmetry of Eu^{3+} ions. A higher asymmetric ratio (R > 1) indicates lower symmetry in the region surrounding Eu^{3+} ions, explaining the dominance of the red color. In the present study, the asymmetric ratio was calculated to be higher than 1. The calculated data are in good agreement with experimental and theoretical results (Table 2) and show good consistency with other Eu^{3+}-doped phosphors reported in the literature [31,56]. The high asymmetric ratio indicates that Eu^{3+}-doped MgO:0.05Ag^+ samples can emit red light. These findings are consistent with the observed increase in the $^5D_0 \rightarrow {}^7F_2$ transition intensity in the PL spectra and confirm the effect of increasing Eu^{3+} concentration on both spectroscopic and structural properties. Another important parameter is the radiative transition probability A(J,J′) term. The radiative transition probability A ($^5D_0 \rightarrow {}^7F_2$), shows an increasing trend with Eu^{3+} concentration; starting at 357.58 s^{-1} for a concentration of 0.005, it peaks at 415.39 s^{-1} for a concentration of 0.07. This increase confirms the enhanced sensitivity of the $^5D_0 \rightarrow {}^7F_2$ transition, which is typically associated with asymmetric local environments and increased covalency.

Another important parameter in the Judd–Ofelt theory, the branching ratio (β), quantitatively expresses the probability of radiative transitions between specific energy levels and is calculated by multiplying the radiative transition probability A(J, J′) by the total radiative probability ΣA(J, J′) and then multiplying the result by 100. The calculated β values are summarized in Table 2. For the MgO:0.05Ag^+:Eu^{3+} phosphor series, the branching ratio of the highly sensitive electric dipole transition $^5D_0 \rightarrow {}^7F_2$ increases slightly with Eu^{3+} concentration. Branching ratios above 50 % in all samples were generally favorable for stimulated emission processes and highlight the importance of a potential laser emission transition [49,57]. The branching ratio indicates the ratio of the emission area of a specific transition to the total area covered by various transitions under the emission peaks. The experimental branching ratios calculated from the relative areas of the $^5D_0 \rightarrow {}^7F_J$ (J = 1, 2) transitions are in good agreement with the theoretical ratios. These findings provide valuable information about the structural and optical behavior of Eu^{3+}-doped MgO:0.05Ag^+ phosphors, thereby providing important insights for the optimization of luminescent materials in optical applications.

Quantum efficiency (η_{QE}) represents the ratio of excited Eu^{3+} ions which undergo radiative decay and is determined using the Judd–Ofelt (JO) formalism. η_{QE} and W_{NR} values are defined as the ratio of the experimental lifetime (τ_{exp}) to the radiative lifetime (τ_r) and are therefore expressed by Equation (13) [58,59]:

Table 1
Squared matrix elements for transitions $^5D_0 \rightarrow {}^7F_j$ (j = 2, 4 and 6) of Eu^{3+} ions.

Transition	$(0\ \|U^{(2)}\|\ J')$	$(0\ \|U^{(4)}\|\ J')$	$(0\ \|U^{(6)}\|\ J')$
$^5D_0 \rightarrow {}^7F_2$	0.0032	0	0
$^5D_0 \rightarrow {}^7F_4$	0	0.0023	0
$^5D_0 \rightarrow {}^7F_6$	0	0	0.0002

Table 2
Judd–Ofelt parameters ($\Omega_2$and Ω_4), radiative transition probabilities (A (J, J')), and branching ratios (β_{cal}) of the MgO:xEu^{3+}phosphors.

Eu^{3+} conc. (x wt.%)	Ω_2 (10^{-20} cm^2)	Ω_4 (10^{-20} cm^2)	A(J,J')		β (%) Exp.	β (%) Theo.	R Exp.	R Theo.
0.005	7.99	3.34	$^5D_0 \rightarrow {}^7F_1$	63.03	13.95	11.93	5.138	5.673
			$^5D_0 \rightarrow {}^7F_2$	357.58	71.67	67.70		
			$^5D_0 \rightarrow {}^7F_4$	107.56	14.38	20.36		
0.01	8.33	3.05	$^5D_0 \rightarrow {}^7F_1$	63.15	13.75	11.80	5.335	5.919
			$^5D_0 \rightarrow {}^7F_2$	373.78	73.34	69.85		
			$^5D_0 \rightarrow {}^7F_4$	98.20	12.92	18.35		
0.02	8.54	3.16	$^5D_0 \rightarrow {}^7F_1$	63.08	13.43	11.51	5.471	6.070
			$^5D_0 \rightarrow {}^7F_2$	382.90	73.47	69.89		
			$^5D_0 \rightarrow {}^7F_4$	101.85	13.10	18.59		
0.03	8.62	3.20	$^5D_0 \rightarrow {}^7F_1$	63.06	13.31	11.41	5.522	6.127
			$^5D_0 \rightarrow {}^7F_2$	386.35	73.53	69.92		
			$^5D_0 \rightarrow {}^7F_4$	103.17	13.16	18.67		
0.05	9.22	3.42	$^5D_0 \rightarrow {}^7F_1$	63.03	12.62	10.76	5.783	6.549
			$^5D_0 \rightarrow {}^7F_2$	412.82	74.14	70.47		
			$^5D_0 \rightarrow {}^7F_4$	109.96	13.24	18.77		
0.07	9.23	3.60	$^5D_0 \rightarrow {}^7F_1$	63.32	12.38	10.64	5.969	6.559
			$^5D_0 \rightarrow {}^7F_2$	415.39	73.89	69.81		
			$^5D_0 \rightarrow {}^7F_4$	116.26	13.73	12.38		

Table 3
Radiative lifetimes (τ_r), experimental lifetimes (τ_{exp}), non-radiative rates (W_{NR}) quantum efficiencies (η_{QE}) for MgO:Ag0.05,xEu^{3+} (x = 0.005–0.07) phosphors.

Eu^{3+} conc. (x wt.%)	τ_r(ms)	τ_{exp}(ms)	W_{NR} (s^{-1})	η_{QE}(%)
0.005	1.893	1.149	3.42×10^{-4}	60.69
0.01	1.868	1.457	1.51×10^{-4}	77.97
0.02	1.825	1.521	1.09×10^{-4}	83.38
0.03	1.809	1.358	1.68×10^{-4}	76.64
0.05	1.707	1.313	1.83×10^{-4}	76.16
0.07	1.681	1.134	2.86×10^{-4}	67.52

Table 4
CIE, coordinates of phosphors doped with Eu^{3+} at various concentrations and CCT (Color Correlation Temperature) comparisons.

Composition	CIE chromaticity coordinates		CCT value	CP
	x	y	(K)	(%)
(A) MgO:0.05Ag^+,0.005Eu^{3+}	0.6285	0.3464	2116	83.95
(B) MgO:0.05Ag^+,0.01Eu^{3+}	0.6287	0.3439	2166	83.97
(C) MgO:0.05Ag^+,0.02Eu^{3+}	0.6517	0.3474	2346	90.54
(D) MgO:0.05Ag^+,0.03Eu^{3+}	0.6443	0.3460	2293	88.42
(E) MgO:0.05Ag^+,0.05Eu^{3+}	0.5912	0.3447	1823	73.35
(F) MgO:0.05Ag^+,0.07Eu^{3+}	0.5720	0.3403	1746	67.86

Table 5
Summary on luminescence properties of MgO:0.05Ag^+,0.02Eu^{3+} and reported Eu^{3+}-doped phosphor materials.

Composition	CIE chromaticity coordinates		CCT value	CP	
	x	y	(K)	%	Ref
MgO:0.05Ag^+,0.02Eu^{3+}	0.6517	0.3474	2346	90.54	This work
$Ba_3Y_4O_9$:0.03Eu^{3+}	0.6345	0.3527	*1100*	*96.30*	[63]
NSMP: 0.09Eu^{3+}	0.6724	0.3274	*3258*	*95*	[64]
$Y_2SrAl_4SiO_{12}$: 0.02Eu^{3+}	0.6346	0.3650	*2092*	*90*	[65]
$SrGa_4O_7$:0.3Eu^{3+}	0.6442	0.3499	*2489*	*99.92*	[66]
Ba_2SrWO_6:0.1Eu^{3+}	0.6273	0.3721	*1956*	*87.35*	[67]

$$\eta_{QE} = \frac{A_r}{A_r + A_{nr}} = \frac{\tau_{exp}}{\tau_r}, W_{NR} = \tau_{exp}^{-1} - \tau_r^{-1} \quad (13)$$

where τ_r is estimated from the total spontaneous emission probabilities (A_r) calculated with the JO parameters, and $\tau = A_r + A_{nr}$ is calculated from time-resolved photoluminescence measurements under 349 nm excitation observed at 617 nm. The calculated radiative lifetimes (τ_r), experimental lifetimes (τ_{exp}), and quantum efficiencies (η_{QE})and non-radiative rates (W_{NR}) obtained for all Eu^{3+} doped samples are presented in Table 3. The slight difference between τ_{exp} and τ_r is primarily due to the nonradiative relaxation W_{NR} (s^{-1}) of excited Eu^{3+} ions. This nonradiative decay occurs due to the interaction of Eu3+ ions with vibrations in the host matrix and leads to their transition to lower energy states by emitting multiple phonons, a phenomenon known as multiple phonon relaxation. As the Eu3+ content increases up to 0.02 doping, W_{NR} decreases while η_{QE} reaches its maximum value of 83.38 %. This results in a substantially higher radiation rate and improved efficiency. As the Eu^{3+} content exceeds ~0.02, a slight decrease in ηQE is observed, from 83.38 % (x = 0.02) to 67.52 % (x = 0.07). This decrease is attributed to increased cross-relaxation and multipolar quenching phenomena between activator ions that are close to each other. This supports the strengthening of phonon-assisted non-radiative channels.

3.4.4. CIE analysis

The photometric properties of luminescent materials are important parameters for the determination of their suitability for various lighting and imaging applications. Fig. 7 demonstrates the photometric quantities of Ag^+ and Eu^{3+} co-doped MgO phosphors were ascertained using the Commission Internationale de l'Eclairage (CIE) 1931 colour diagram. Table 4 summarizes the CIE parameters of Ag^+ and Eu^{3+} co-doped MgO phosphors, showing that the CIE chromaticity coordinates are in the red emission region and confirming the red colour emission. At an excitation wavelength of 349 nm, the sample with the highest intensity (MgO:0.05Ag^+,0.02Eu^{3+}) shows coordinates of (0.6517, 0.3474).

Color-correlated temperature (CCT) is another key feature of smart lighting devices. The colour temperature of a light source is the key to its classification as warm, neutral or cool. Typically, a colour-temperature of approximately 6500 K is regarded as cool light, while a colour temperature of less than 4500 K is considered warm light. Warm light or light with a low CCT is better for the human eye. CIE parameters such as color coordinates (x, y) and color correlated temperature (CCT) were calculated to characterize the emitted color [60]. Color correlated temperature (CCT) was calculated using the McCamy empirical formula [61].

$$CCT = -437n^3 + 3601n^2 - 6861n + 5514.31$$

where $n=(x-x_e)/(y-y_e)$ and the color epicenter is located at $x_e = 0.3320$ and $y_e = 0.1858$. Therefore, the correlated color temperature (CCT) was calculated for MgO:0.05Ag^+,0.02Eu^{3+} phosphor samples using the above equation. The CCT value calculated for different Eu^{3+} concentrations was approximately 1746–2346 K.

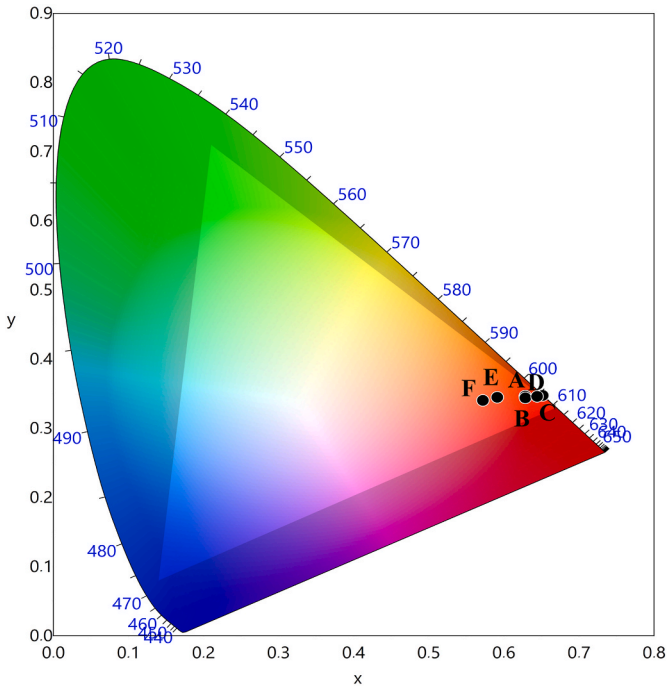

Fig. 7. The CIE chromaticity coordinates of MgO:0.05Ag^{+}, xEu^{3+} (x = 0.01–0.07) phosphors.

The calculated CCT values fall within the warm light region, confirming that the proposed sample is suitable for the production of warm WLEDs. To accurately characterize the light sources, the color purity (CP) of the emitted color was calculated using the following formula [62]:

$$Color\ Purity = \frac{\sqrt{(x-x_i)^2+(y-y_i)^2}}{\sqrt{(x_d-x_i)^2+(y_d-y_i)^2}} \times 100\% \quad (14)$$

where, (x,y) are the CIE color coordinates of the proposed samples, (x_d, y_d) are the color coordinates of the dominant wavelength, and (x_i,y_i) are the coordinates of the standard white light source. Color purity is an important property in color science that measures how vivid or saturated a color appears. It is expressed on a scale ranging from 0 % (achromatic white) to 100 % (pure spectral color). In the present study, the color purity value of MgO:0.05Ag^{+},0.02Eu^{3+} nano-phosphor, which exhibits the highest emission intensity of the material, has been determined. Table 5 summarizes the color purity comparisons of previously reported nano phosphors. Compared to our study on MgO:0.05Ag^{+}, Eu^{3+}, we observe better results here. These results clearly show that the monochromatic nature of the emitted light improves as the Eu^{3+} ion concentration increases up to 2 wt%. The color purity indicators indicate that the synthesized phosphor emits stable and bright red light with excellent color stability. Therefore, depending on the Eu^{3+} doping concentration in MgO:0.05Ag^{+} nano-phosphors, the PL emission and color purity have been improved, and the findings indicate the potential future applications of Eu^{3+}-doped MgO:0.05Ag^{+} in w-LEDs and warm solid-state lighting.

3.4.5. Thermal stability analysis

One of the most important parameters in the applications of photoluminescence is its thermal stability. Temperature increases cause a decrease in the photoluminescence performance of doped rare earth phosphors, a phenomenon referred to as temperature quenching. Therefore, the thermal stability of photoluminescence is considered to be one of the most important parameters in the application of phosphors. Higher temperatures lead to more frequent non-radiative hopping between luminescent centers, resulting in a decrease in luminescence intensity [68]. To investigate the thermal stability of MgO:0.05Ag^{+}, 0.02Eu^{3+} phosphors, the intensity changes of the emission spectra were measured under 349 nm excitation light in the temperature range of 300–550 K, as shown in Fig. 8(a–c). The initial temperature was 300 K, the maximum temperature was 500 K, and the emission spectra were measured at 40 K intervals.

Fig. 8 (b) shows the normalized results and indicates that the emission intensity under 349 nm excitation remains at approximately 83 % of the value at room temperature (300 K) when the temperature reaches 420K, representing a slight decrease compared to room temperature. This indicates that MgO:0.05Ag^{+},0.02Eu^{3+} possesses exceptional thermal stability properties. To further detail the thermal stability of the nanophosphor, the Arrhenius activation model can be used to evaluate the activation energy of the phosphor [69,70].

$$I_T = I_0\left(1 + Aexp\left(-\frac{\Delta E}{k_B T}\right)\right)^{-1} \quad (15)$$

where, A is a constant, I_0 represents the light intensity at room temperature, and I_T represents the light intensity measured at temperature T. The Boltzmann constant is denoted by k_B (8.63×10^{-5} eV/K). The Arrhenius approach can be modified as shown below; this equation shows the relationship between $\ln(I_0/I_T\text{-}1)$ and $1/k_BT$. The relationship between $\ln(I_0/I_T\text{-}1)$ and k_BT is shown in Fig. 8(d). The linear curve in the figure can be obtained by fitting the data below the excitation wavelength linearly, and the corresponding slope of the curve represents the activation energy. Specifically, the activation energy of the nano phosphor synthesized under 349 nm excitation is 0.209 eV. Table 6 summarizes the thermal stability of MgO:0.05Ag^{+},0.02Eu^{3+} phosphors with different phosphor series, and the findings highlight that MgO:0.05Ag^{+},0.02Eu^{3+} phosphors exhibit good thermal stability. Furthermore, as summarized in Table 7, which presents a comparative analysis of the optical properties of Eu^{3+}-doped phosphors, such luminescence modifications are crucial for understanding the potential of co-doped systems. This work, which combines enhanced photocatalytic degradation efficiency, superior antibacterial activity, and strong luminescence properties in a single system, aims to position MgO doped with Ag^{+}/Eu^{3+} as a multifunctional nanomaterial with potential applications in environmental remediation, biomedical coatings, and optoelectronic devices.

3.5. Antibacterial activity

The samples containing MgO exhibited antibacterial activity against *E. coli* at all concentrations; however, no antibacterial activity was detected against *S. aureus*. The inhibition zone diameters produced by MgO compounds against both bacterial strains are summarized in Table 8, while representative images of the zones are illustrated in Fig. 9.

The release of free Mg^{2+} ions from phosphors is considered the primary driver of reactive oxygen species (ROS) generation (see Fig. 9). The resulting excessive oxidative stress overwhelms the bacterial antioxidant defenses, leading to cellular damage. Correspondingly, the leakage of proteins, carbohydrates, and lipids due to membrane disruption has been quantified, with the extent of leakage observed to vary according to the bacterial cell structure [77,78]. Notably, elevated ROS levels have been reported to confer up to 98 % antibacterial activity against *E. coli* [79].

In the present study, the MgO compounds demonstrated inhibitory activity against *E. coli*, whereas no inhibition was observed against *S. aureus*, consistent with the findings of Li et al. [79]. These results highlight that the antibacterial efficacy of nanoparticles is not solely determined by their size, shape, chemical composition, and surface properties (e.g., hydrophobicity), but also depends on the bacterial species [2].

Suresh et al. (2018) synthesized MgO nanoparticles using *C. pictus*

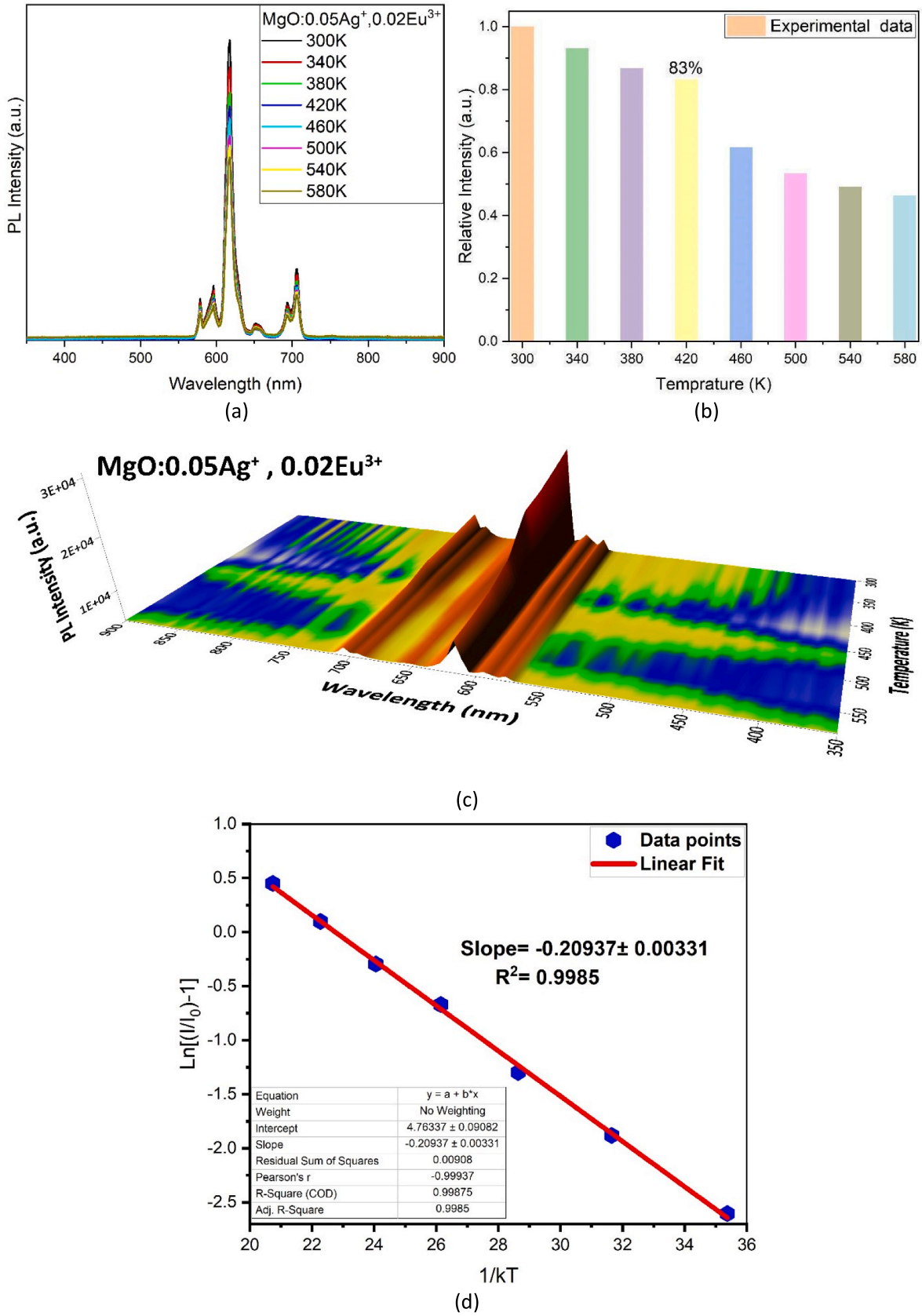

Fig. 8. (a) Temperature-dependent photoluminescence (PL) emission spectra of the MgO:0.05Ag^{+}, 0.02Eu^{3+} phosphor, measured under fixed excitation conditions in the range of 300–580 K. (b) Normalized luminescence intensity of MgO:0.05Ag^{+},0.02Eu^{3+} phosphor at different temperatures. (c) 3D spectral mapping showing the evolution of emission intensity with increasing temperature from 300 K to 580 K, with a gradual decline in luminescence due to thermal quenching effects. (d) An Arrhenius plot of the MgO:0.05Ag^{+},0.02Eu^{3+} phosphor under 349 nm excitation showing the temperature dependence of the luminescence intensity in the range 300–580 K.

Table 6
The I_{550K}/I_{300K} and ΔE values of the related phosphors.

phosphor	I420K/I300K	ΔE(eV)	*Ref.*
$MgO:0.05Ag^{+},0.02Eu^{3+}$	83 %	0.209	This work
$Ba_3Y_4O_9:Eu^{3+}$	85 % (420K)	0.375	[63]
$BlIO:Eu^{3+}$	61 %(423K)	0.188	[71]
SLG: $0.3Eu^{3+}$	60.7 % (423K)	0.299	[72]
$Sr_3CaNb_2O_9$: Eu^{3+}	72.5 % (420K)	0.184	[73]
$InGaZnO_4:Eu^{3+}$	73.5 % (420 K)	0.270	[74]
$NaCaTiTaO_6:Eu^{3+}$	72.41 % (420 K)	0.310	[75]
$CaSrSb_2O_7:Eu^{3+}$	50.69 % (423 K)	0.229 eV	[76]

leaf extract and reported their bactericidal effects, with inhibition zones of 5.50 cm against *S. aureus*, 10 cm against *B. subtilis*, 12.50 cm against *E. coli*, and 15 mm against S. Paratyphi. In a comparative study, He et al. (2018) found that MgO and CuO nanoparticles exhibited significantly higher antibacterial activity against Gram-positive bacteria than against Gram-negative bacteria, likely due to differences in cell membrane structure. Similarly, Akshaykranth et al. [80] demonstrated that MgO nanoparticles possess substantial activity against both Gram-negative and Gram-positive bacteria, with the magnitude of antimicrobial effect being dependent on particle size, shape, and concentration. Supporting this observation, Abinava et al. [20] reported that inhibition zones produced by standard MgO nanoparticles were considerably lower than those produced by HY-MgO nanoparticles.

Interestingly, contrary to He et al. [2], the current study observed that MgO nanoparticles exerted greater activity against *E. coli*, while no measurable inhibition zones were observed for *S. aureus*. This novel finding further supports the notion proposed by Akshaykranth et al. [80] that the antimicrobial activity of MgO nanoparticles is highly dependent on their physicochemical characteristics. Nevertheless, it is plausible that the observed effects may also be influenced by the specific components within the nanoparticles, indicating that further investigations are required to fully elucidate the antibacterial potential of MnO.

The higher antibacterial activity observed against *E. coli* can be explained by fundamental differences in the cell-wall architecture and surface charge properties of Gram negative and Gram positive bacteria. *E. coli*, a Gram negative bacterium, possesses a thin peptidoglycan layer located between the inner membrane and an outer membrane enriched with lipopolysaccharides (LPS). LPS molecules contain abundant negatively charged phosphate groups, which promote strong electrostatic interactions with positively charged antibacterial agents or nanomaterials. These interactions can increase outer-membrane permeability and destabilize the membrane, contributing to the higher susceptibility of Gram-negative bacteria [81]. In contrast, *S. aureus*, a Gram-positive bacterium, has a substantially thicker (20–40 nm) and highly cross-linked peptidoglycan layer. This rigid structure acts as a physical

Table 7
Comparative analysis of the optical characteristics of Eu^{3+}-doped phosphors.

Sample composition	CIE chrom. coordinates	Thermal Stability	Averaged Life time (ms)	Applicaiton potential	Ref
$MgO:0.05Ag^{+},0.02Eu^{3+}$	0.6517,0.3474	83 % (Moderate)	1.521 ms (Moderate)	Red phosphor for warm white LEDs	This work
$Na_2SrMg(PO_4)_2:Eu^{3+}$	0.6720,0.3270	71 % (Moderate)	2.872 ms (slow)	Red phosphor for warm white LEDs	[64]
$Sr_3CaNb_2O_9$: $0.03Eu^{3+}$	0.5985, 0.3968	72.5 % (Moderate)	0.261 ms (Light fast)	Red light-emitting component of WLED	[73]
$CaSrSb_2O_7$: 0.20 Eu^{3+}	0.5870,0.3890	50.69 % (Low moderate)	–	Red phosphor for SSL applications	[76]
$Ba_3Y_4O_9:0.03Eu^{3+}$	0.3460, 0.3480	85 % (Moderate)	2.812 ms (slow)	Red phosphor for high performance WLED	[63]

Table 8
Inhibition zones of the MgO, $MgO:0.05Ag^{+}$ and $MgO:0.05Ag^{+}:xEu^{3+}$ (x = 0.005–0.07 wt) phosphor antibacterial activity against *E. coli* and S.aureus.

MgO Compounds	Codes of MgO compounds in study	Zone diameters against *E. coli* (mm)	Zone diameters against *S. aureus* (mm)
MgO	B0	8	–
$MgO:0.05\ Ag^{+}$	B1	11	–
$MgO:0.05Ag^{+}:0.005Eu^{3+}$	B2	13	–
$MgO:0.05Ag^{+}:0.01Eu^{3+}$	B3	15	–
$MgO:0.05Ag^{+}:0.02Eu^{3+}$	B4	10	–
$MgO:0.05Ag^{+}:0.03Eu^{3+}$	B5	10	–
$MgO:0.05Ag^{+}:0.05Eu^{3+}$	B6	13	–
$MgO:0.05Ag^{+}:0.07Eu^{3+}$	B7	15	–

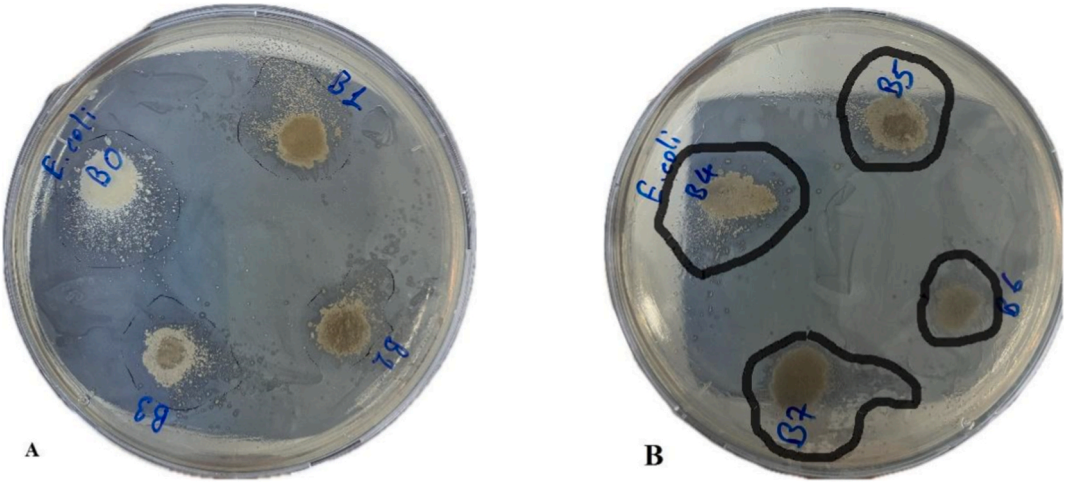

Fig. 9. (A). Inhibition zones of MgO, $MgO:0.05Ag^{+}$, $MgO:0.05Ag^{+},0.05Eu^{3+}$ and $MgO:0.05Ag^{+},0.01Eu^{3+}$ (B). Inhibition zones of $MgO:0.05Ag^{+},0.02Eu^{3+}$, $MgO:0.05Ag^{+},0.03Eu^{3+}$, $MgO:0.05Ag^{+},0.05Eu^{3+}$ and $MgO:0.05Ag^{+},0.07Eu^{3+}$.

barrier that limits penetration of antibacterial agents to the cytoplasmic membrane. Although teichoic acids in Gram-positive cell walls also confer a net negative charge, the density of accessible anionic sites is lower than in the LPS-rich outer membrane of Gram-negative bacteria, resulting in weaker electrostatic attraction. Consequently, the robust and multilayered cell wall of Gram-positive bacteria reduces antibacterial efficacy [82]. These structural and surface-charge differences provide a clear explanation for the stronger antibacterial performance observed against *E. coli* compared to *S. aureus*.

3.6. Photocatalytic comparisons of MgO and different dopants of MgO NPs

In this study, the photocatalytic activity of MgO/MnO_2 phosphors was evaluated by the photocatalytic degradation of CV (crystal violet) solution at 583 nm under visible light irradiation for a period of 75 min. The experiment was initiated in a dark room, and the light irradiation time (0–75 min) was regularly analyzed at room temperature. The study also investigated the significant effects of various physical parameters,

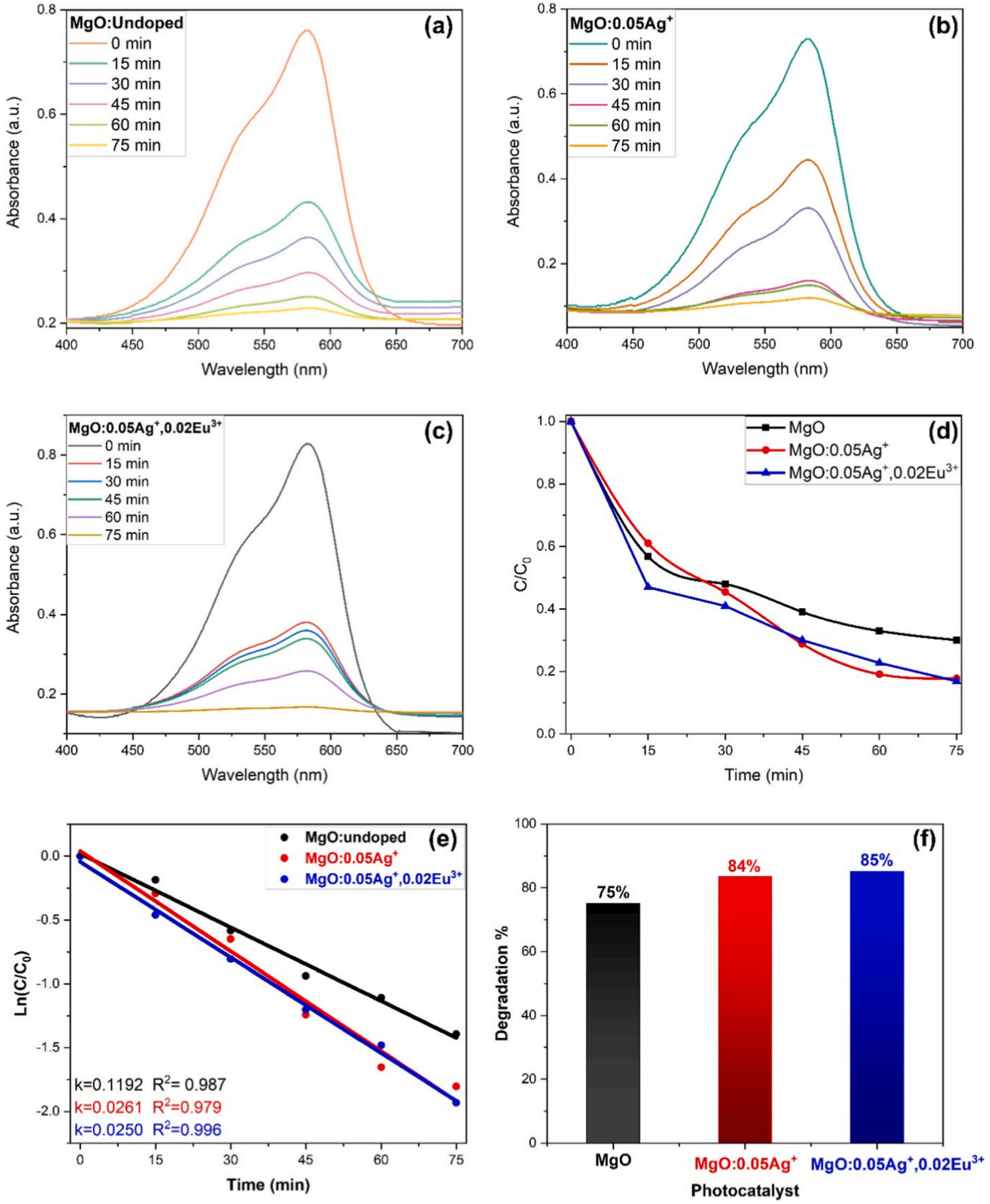

Fig. 10. UV–vis absorbance as function of time of (a) MgO, (b) MgO:0.05Ag^{+} and (c) MgO:0.05Ag^{+}:0.02Eu^{3+} photocatalyst under sunlight irradiation (dose: 50 mg/L; CV concentration: 1x10^{-5} M; ambient temperature = 30–35 °C) (d)The variation of photodegradation with time, (e) pseud-first-order kinetics (*f*) and the degradation % of CV dye.

such as time, catalyst type, and solution, on the degradation process. A gradual decrease in the absorption intensity of CV under light was observed, and the degradation of the dye on the surfaces of MgO, MgO:0.05Ag^{+}, and MgO:0.05Ag^{+},0.02Eu^{3+} was recorded. The photocatalytic degradation of the CV dye was investigated to determine the percentage of adsorbed photocatalyst and compared with adsorption analysis. To examine the degradation stages in detail, the experiment was conducted under sunlight in the presence of the photocatalyst. The data indicate that MgO:0.05Ag^{+} and MgO:0.05Ag^{+},0.02Eu^{3+} phosphors provide the highest dye degradation compared to MgO. The dye photocatalytic degradation percentage occurred in the following order: MgO:0.05Ag^{+},0.02Eu^{3+} (84 %) > MgO:0.05Ag^{+} (83 %) > MgO (75 %). The highest efficiency of MgO:0.05Ag^{+},0.02Eu^{3+} may be related to its excellent visible light absorption capacity. The graphs in Fig. 10(a-f) compare the photocatalytic efficiency of MgO, MgO:0.05Ag^{+}, and MgO:0.05Ag^{+},0.02Eu^{3+} against CV dye under visible light. The photocatalytic degradation processes of most organic/inorganic pollutants follow the Langmuir–Hinshelwood kinetic model, which assumes the single-layer adsorption of reactants or products. This is generally expressed by the following equation:

$$r = -\frac{d_c}{d_t} = \frac{kKC}{(1+KC)}$$

where, the reaction rate (r), the reaction rate constant (k), the adsorption coefficient of the adsorbate at time t (K: typically in mM^{-1}), and the initial concentration of the contaminant in the solution are dependent and the equation transforms into pseudo-first-order kinetics The degradation reaction process shows good agreement with the pseudo-first-order reaction kinetic model:

$$ln\ ln\frac{A_0}{A_t} = ln\ ln\frac{C_0}{C_t} = kt$$

where, A and C are the absorbance and concentration at time 0 and any time t (A = αC), and k is the pseudo-first-order rate constant obtained from the linear ln(C_0/C_t vs. t) plots (min^{-1}). The fit of the data to the pseudo-first-order reaction kinetics was confirmed for all photocatalysts with a regression coefficient $R^2 \geq 0.97$. The higher photocatalytic performance of the MgO:0.05Ag^{+},0.02Eu^{3+} composite is evidenced by higher reaction rate constants and very short $t_{1/2}$ ($t_{1/2}$ = ln2/k) (Table 9). The maximum k values (0.0261 min^{-1} and 0.025 min^{-1}) obtained for the MgO:0.05Ag^{+} and MgO:0.05Ag^{+},0.02Eu^{3+} composites are approximately 2.1 times higher than that of MgO under the same conditions (Table 9). This excellent performance can be attributed to the effective separation of photogenerated electron pairs within the composite. The findings point to the fact that Ag^{+} and Ag^{+}/Eu^{3+}-doped MgO nanomaterials exhibit higher photoactivity against CV elimination under sunlight [83].

3.6.1. Photocatalytic comparisons of MgO and MgO NP variants

Fig. 11 represents the possible mechanism of paint degradation of MgO and its variants under visible light irradiation. The valence band (VB) and conduction band (CB) edge potentials of pure MgO were calculated using the following equations (16) and (17) [84].

$$E_{VB} = X - E^{e} + 0.5E_g \quad (16)$$

$$E_{CB} = E_{VB} - E_g \quad (17)$$

Table 9
Kinetic parameters of CV dye degredation.

Sample	k(min^{-1})	$t_{1/2}$ (min)	R^2
MgO	0.0119	361	0.9877
MgO:0.05 Ag^{+}	0.0261	26	0.9799
MgO:0.05Ag^{+}:0.02Eu^{3+}	0.025	27	0.9963

Here, E_{VB} and E_{CB} represent the valence and conduction band potentials of the semiconductor, respectively, X and Eg represent the electronegativity and band gap energy of the semiconductor, respectively, and E^{e} represents the energy of free electrons in the hydrogen scale (~4.5 eV). The absolute electronegativity of pure MgO is 5.68 eV [85]. The VB and CB edge potentials of pure MgO were calculated to be +3.18 and −0.82 eV, respectively.

$$Photocatalyst + h\nu \rightarrow h^{+} + e^{-}$$

$$e^{--} + O_2 \rightarrow O_2^{-\cdot}$$

$$h^{+} + H_2O \rightarrow OH + H^{+}$$

$$O_2^{-\cdot} + H^{+} \rightarrow HO_2^{\cdot}$$

$$2HO_2^{\cdot} + H_2O_2 \rightarrow O_2$$

$$H_2O_2 \rightarrow 2OH\cdot$$

$$\cdot OH + CV\ dye \rightarrow CO_2 + H_2O$$

It is necessary to identify significant findings in the background of the photocatalytic degradation of CV dye on MgO, MgO:0.05Ag^{+}, and MgO:0.05Ag^{+},0.02Eu^{3+} photocatalysts. The photo-color loss of fast orange-red dye is photosensitized under the influence of UV or visible light irradiated onto the surface of the photocatalyst. When the photocatalyst is excited by light, most often a visible light source, it absorbs photons with energy equal to or greater than the band gap energy. This energy excites electrons from the valence band to the conduction band, resulting in the formation of electron-hole pairs (e^{-}/h^{+}). Photogenerated electrons (e−) in the conduction band are responsible for the formation of reactive oxygen species, such as superoxide radicals (•O_2-), by reducing oxygen molecules (O_2) in the solution. Similarly, photo-generated holes (h^{+}) in the valence band produce hydroxyl radicals (•OH) by oxidizing water (H_2O) or hydroxyl ions (OH^{-}) on the catalyst surface. These reactive species (•O_2- and •OH) are highly oxidative and interact intensely with CV dye molecules, breaking down their complex structures into smaller and less harmful molecules. Comparisons of various nanomaterials on photocatalytic studies regarding photocatalytic degradation are given in Table 10. Similar luminescence-catalysis synergies have also been reported in other Ag^{+}/Eu^{3+} co-doped oxide photocatalysts, where Eu^{3+}-induced optical transitions and Ag^{+}-related charge separation collectively enhance the generation of reactive oxygen species and improve dye degradation efficiency [35,86,87].

The structural, morphological, optical, and functional analyses of the synthesized MgO, Ag-doped MgO, and Ag/Eu co-doped MgO phosphors reveal a strong correlation between dopant incorporation and multifunctional performance. XRD results confirmed that the cubic MgO lattice was retained in all samples, while new reflections corresponding to Eu_2O_3 and metallic Ag phases appeared in the co-doped systems. This indicates limited solubility of the dopant ions in the host lattice and shows that phase segregation contributes to the overall physicochemical behavior of the nanomaterials. Supporting these findings, FTIR spectra showed Mg-O stretching vibrations together with surface hydroxyl features, confirming the presence of intrinsic MgO bonding and surface sensitivity.

SEM micrographs further demonstrated the effects of doping on morphology. While pure MgO phosphors were irregular and randomly distributed, Ag^{+} doping induced spheroidization and localized agglomeration. In the Ag^{+}/Eu^{3+} co-doped samples, these effects were more pronounced, leading to layered agglomeration in random orientations. These microstructural changes suggest that Eu^{3+} incorporation promotes local distortions and surface reorganization which are closely related to the functional outcomes of the material.

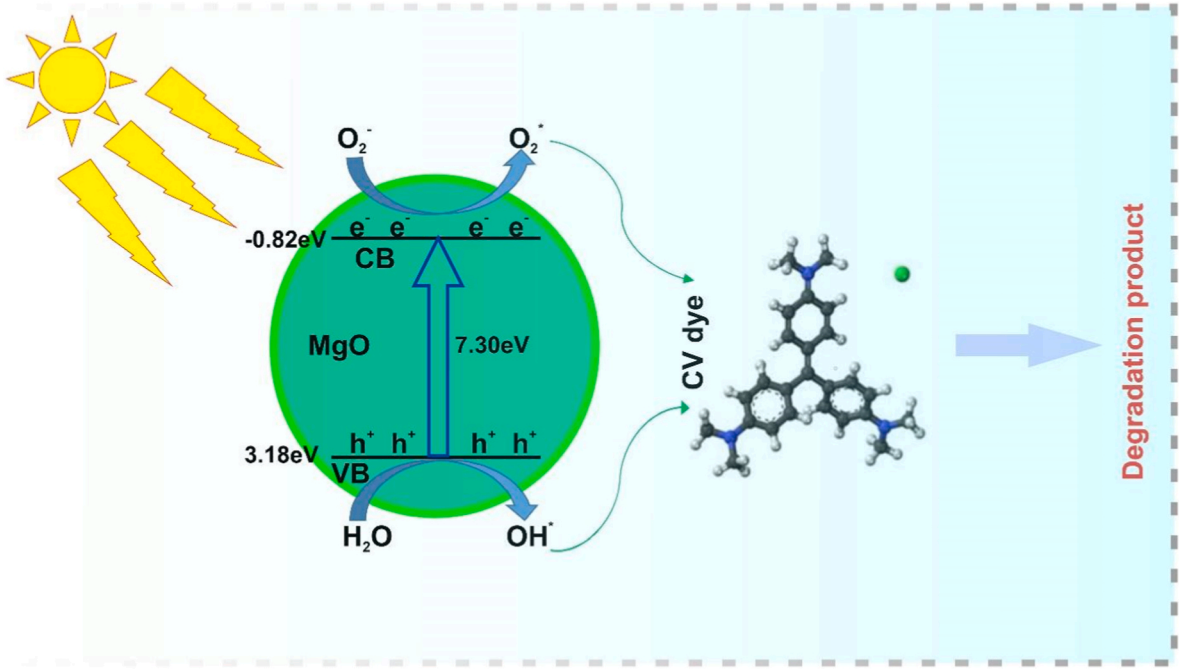

Fig. 11. Photoexcited electron-hole separation of CV on MgO under visible light irradiation, representing the degradation mechanism of transport processes.

Table 10
A comparative study of the photocatalytic degradation performance of various photocatalysts.

Photocatalyst	Dye	Time (min)	Degradation %	Reference
MgO	Crystal Voilet	75	75	This work
MgO:0.05 Ag^{+}	Crystal Voilet	75	84	This work
MgO:0.05Ag^{+}:0.02Eu^{3+}	Crystal Voilet	75	85	This work
Ag doped MgO	Methylene Blue	120	90.18	[12]
Bi_2O_3/MgO/Fe_2O_3	Fast Orange Red	120	82	[88]
MgO@ZrO_2@g-C_3N_4	Alizarin red	60	92.1	[89]
MgO/g-C_3N_4	Crystal Voilet	60	60	[85]
MgO-CeO_2-Fe_3O_4@JB	Niagara blue	25	97.23	[90]
MgO/TiO_2/Ag	Methylene Blue	8	90	[91]
MgO	Malachite Green, Congo red	120	98. 95	[92]
MgO	Methylene Blue	120	90	[93]

Photoluminescence studies revealed characteristic Eu^{3+} emission bands, with the most intense transition observed at 617 nm. The emission intensity increased with Eu^{3+} concentration up to 2 wt%, after which concentration quenching became dominant. This quenching behavior, attributed to multipolar interactions, demonstrates the critical balance between activator concentration and luminescence efficiency. Lifetime measurements supported this trend: undoped MgO showed weak and rapid decay, while co-doping significantly increased lifetimes, indicating the activation of radiative pathways. Judd-Ofelt analysis provided further confirmation, with higher Ω_2 values compared to Ω_4 across all samples, pointing to low-symmetry local environments and a more covalent nature of Eu-O bonds. These findings are consistent with the high asymmetry ratios ($R > 1$) observed, which explain the dominance of red emission.

The CIE chromaticity coordinates of the optimized MgO:Ag^{+},Eu^{3+} composition (0.6517, 0.3474) placed the emission firmly in the red region. The correlated color temperature in the range of 1746–2346 K confirmed warm light characteristics, while the color purity exceeded 90 percent at optimal Eu^{3+} concentration. Together with the excellent thermal stability results, where 83 percent of the initial emission was retained at 420 K with an activation energy of 0.209 eV, these properties demonstrate the suitability of the material for warm white LED and solid-state lighting applications.

Biological assays revealed species-selective antibacterial activity. All MgO-based phosphors inhibited the growth of *E. coli*, whereas no inhibition was observed against *S. aureus*. Ag^{+} doping enhanced inhibition compared to undoped MgO, and Eu^{3+} incorporation produced a variable response, with the highest activities recorded at 0.01 and 0.07 Eu concentrations. These results suggest that the antibacterial effect is mediated by both ionic release and reactive oxygen species formation, and that surface modifications due to doping play a decisive role in determining activity levels.

Photocatalytic degradation studies further emphasized the multifunctional nature of the co-doped systems. Both Ag^{+}-doped and Ag^{+}/Eu^{3+} co-doped MgO exhibited higher efficiencies in crystal violet degradation (83–84 %) compared to pure MgO (75 %). Kinetic analysis confirmed pseudo-first-order behavior, with rate constants of approximately 0.025–0.026 min^{-1} for doped samples, more than double that of undoped MgO. This enhancement is attributed to the synergistic effects of Ag, which improves charge separation, and Eu^{3+}, which promotes energy transfer, thereby reducing electron-hole recombination and accelerating dye degradation.

Overall, these findings suggest that Ag^{+} and Eu^{3+} co-doping significantly improves the multifunctional performance of MgO phosphors. The optimized materials exhibit structural stability, efficient red luminescence, high color purity, strong thermal resistance, selective antibacterial activity, and enhanced photocatalytic efficiency. This combination of properties highlights their potential for practical applications in environmental remediation, lighting technologies, and other advanced functional systems.

4. Conclusions

In this study, MgO, Ag^{+}-doped MgO, and Ag^{+}/Eu^{3+} co-doped MgO phosphors were successfully synthesized using a controlled co-precipitation method and their structural, optical, antibacterial, and photocatalytic properties were systematically evaluated. Structural analyses confirmed the formation of cubic MgO along with Eu_2O_3 and metallic Ag phases in the co-doped samples, while microscopic

observations revealed significant morphology evolution toward spheroidized and layered agglomerates with Ag^{+} and Eu^{3+} doping.

Photoluminescence investigations demonstrated strong Eu^{3+}-related emissions, with the most intense band observed at 617 nm, and a maximum luminescence efficiency achieved at 2 wt% Eu^{3+} before concentration quenching set in. Judd-Ofelt analysis revealed low-symmetry environments and strong covalent Eu-O bonding, supporting efficient red emission with high color purity (>90 %) and thermal stability, retaining 83 % of initial intensity at 420 K. These findings highlight the suitability of the optimized composition as a red phosphor for warm white LED and solid-state lighting applications.

The antibacterial studies indicated species-selective behavior, with all samples exhibiting inhibitory activity against *E. coli* but none against *S. aureus*. Ag^{+} doping enhanced antibacterial effects, while Eu^{3+} co-doping produced a non-linear variation, with particularly strong inhibition at specific Eu^{3+} concentrations. Photocatalytic dye degradation experiments further established the multifunctional advantage of doping, with MgO:Ag^{+} and MgO:Ag^{+},Eu^{3+} achieving significantly higher efficiencies (83–84 %) compared to pure MgO (75 %). Kinetic analyses confirmed pseudo-first-order behavior with rate constants more than double those of undoped MgO, attributable to enhanced charge separation and suppressed electron-hole recombination facilitated by the synergistic action of Ag and Eu.

Overall, these findings suggest that Ag^{+} and Eu^{3+} co-doping of MgO phosphors provides a promising strategy to simultaneously achieve enhanced luminescence, excellent colorimetric properties, superior thermal stability, strong antibacterial activity, and improved photocatalytic degradation performance. These multifunctional attributes underscore the potential of the synthesized nanomaterials for practical applications in environmental remediation, antibacterial systems, and advanced optoelectronic devices.

CRediT authorship contribution statement

Remziye Tulek: Visualization, Software, Project administration, Methodology. **Ali Teke:** Visualization, Methodology. **Guler Yagiz Erdemir:** Visualization, Software, Methodology. **Orkun Babacan:** Software, Formal analysis. **Fatma Unal:** Methodology, Conceptualization. **Mustafa Burak Coban:** Writing – review & editing, Writing – original draft, Supervision, Methodology, Conceptualization.

Declaration of competing interest

The authors declare that they have no known competing financial interests or personal relationships that could have appeared to influence the work reported in this paper.

Acknowledgement

The authors thank to the Research Funds of Balikesir University (Grant No. BAP-2024/038) for the financial support and Balikesir University, Science and Technology Application and Research Center (BUBTAM) for the use of the Photoluminescence Spectrometer.

Data availability

Data will be made available on request.

References

[1] N.-Y.T. Nguyen, N. Grelling, C.L. Wetteland, R. Rosario, H. Liu, Antimicrobial activities and mechanisms of magnesium oxide nanoparticles (nMgO) against pathogenic bacteria, yeasts, and biofilms, Sci. Rep. 8 (2018) 16260, https://doi.org/10.1038/s41598-018-34567-5.

[2] Y. He, S. Ingudam, S. Reed, A. Gehring, T.P. Strobaugh, P. Irwin, Study on the mechanism of antibacterial action of magnesium oxide nanoparticles against foodborne pathogens, J. Nanobiotechnol. 14 (2016) 54, https://doi.org/10.1186/s12951-016-0202-0.

[3] A. Fouda, A.M. Eid, M.A. Abdel-Rahman, E.F. EL-Belely, M.A. Awad, S.E.D. Hassan, Z.E. AL-Faifi, M.F. Hamza, Enhanced antimicrobial, cytotoxicity, larvicidal, and repellence activities of brown algae, cystoseira crinita-Mediated green synthesis of magnesium oxide nanoparticles, Front. Bioeng. Biotechnol. 10 (2022) 1–14, https://doi.org/10.3389/fbioe.2022.849921.

[4] D.-M. Radulescu, I.A. Neacsu, B.S. Vasile, V.-A. Surdu, O.-C. Oprea, R.-D. Trusca, C. Chircov, R.C. Popescu, C.-I. Ilie, L.-M. Ditu, V. Drumea, E. Andronescu, Green-synthesized MgO nanoparticles: structural insights and antimicrobial applications, Int. J. Mol. Sci. 26 (2025) 9021, https://doi.org/10.3390/ijms26189021.

[5] N.T.T. Nguyen, L.M. Nguyen, T.T.T. Nguyen, U.P.N. Tran, D.T.C. Nguyen, T. Van Tran, A critical review on the bio-mediated green synthesis and multiple applications of magnesium oxide nanoparticles, Chemosphere 312 (2023) 137301, https://doi.org/10.1016/j.chemosphere.2022.137301.

[6] H.C.S. Perera, V. Gurunanthanan, A. Singh, M.M.M.G.P.G. Mantilaka, G. Das, S. Arya, Magnesium oxide (MgO) nanoadsorbents in wastewater treatment: a comprehensive review, J. Magnesium Alloys 12 (2024) 1709–1773, https://doi.org/10.1016/j.jma.2024.05.003.

[7] J. Lin, N.-Y.T. Nguyen, C. Zhang, A. Ha, H.H. Liu, Antimicrobial properties of MgO nanostructures on magnesium substrates, ACS Omega 5 (2020) 24613–24627, https://doi.org/10.1021/acsomega.0c03151.

[8] K. Karthik, S. Dhanuskodi, C. Gobinath, S. Prabukumar, S. Sivaramakrishnan, Fabrication of MgO nanostructures and its efficient photocatalytic, antibacterial and anticancer performance, J. Photochem. Photobiol. B Biol. 190 (2019) 8–20, https://doi.org/10.1016/j.jphotobiol.2018.11.001.

[9] M.-A. Gatou, N. Bovali, N. Lagopati, E.A. Pavlatou, MgO nanoparticles as a promising photocatalyst towards rhodamine B and rhodamine 6G degradation, Molecules 29 (2024) 4299, https://doi.org/10.3390/molecules29184299.

[10] S. Thakur, I. Thakur, R. Kumar, Doped MgO nanoparticles: enhanced photocatalytic degradation of organic dyes and antioxidant properties, Mater. Sci. Eng. B 322 (2025) 118628, https://doi.org/10.1016/j.mseb.2025.118628.

[11] Z.M. Alaizeri, H.A. Alhadlaq, S. Aldawood, M.J. Akhtar, M.S. Amer, M. Ahamed, Facile synthesis, characterization, photocatalytic activity, and cytotoxicity of ag-doped mgo nanoparticles, Nanomaterials 11 (2021), https://doi.org/10.3390/nano11112915.

[12] P. Panchal, D.R. Paul, S. Gautam, P. Meena, S.P. Nehra, S. Maken, A. Sharma, Photocatalytic and antibacterial activities of green synthesized Ag doped MgO nanocomposites towards environmental sustainability, Chemosphere 297 (2022) 134182, https://doi.org/10.1016/j.chemosphere.2022.134182.

[13] K.N. Sharvani, G. Prasad S, J. Kaewkhao, N. Intachai, S. Kothan, W. Rachniyom, A. Pasha, R. Rajaramakrishna, Optical and structural properties of Eu^{3+} doped $MgO–Li_2O–Na_2O–BaO–B_2O_3$ glasses for scintillating glass applications, Radiat. Phys. Chem. 199 (2022) 110295, https://doi.org/10.1016/j.radphyschem.2022.110295.

[14] P.B. Devaraja, D.N. Avadhani, S.C. Prashantha, H. Nagabhushana, S.C. Sharma, B. M. Nagabhushana, H.P. Nagaswarupa, H.B. Premkumar, MgO:Eu^{3+} red nanophosphor: low temperature synthesis and photoluminescence properties, Spectrochim. Acta Part A Mol. Biomol. Spectrosc. 121 (2014) 46–52, https://doi.org/10.1016/j.saa.2013.10.060.

[15] L. Peng, Y. Wang, Z. Wang, Q. Dong, Multiplesite structure and photoluminescence properties of Eu^{3+} doped MgO nanocrystals, Appl. Phys. A 102 (2011) 387–392, https://doi.org/10.1007/s00339-010-6027-z.

[16] C. hyuck Bae, K.S. Lim, Enhanced visible emission in Eu^{3+} doped glass containing Ag-clusters, Ag nanoparticles, and ZnO nanocrystals, J. Alloys Compd. 793 (2019) 410–417, https://doi.org/10.1016/j.jallcom.2019.04.122.

[17] V. Begum, M.E. Gruner, C. Vorwerk, C. Draxl, R. Pentcheva, Theoretical description of optical and X-ray absorption spectra of MgO including many-body effects. https://doi.org/10.1103/PhysRevB.103.195128, 2021.

[18] P.J. Quinn, B.K. Markey, M.E. Carter, W.J. Donnelly, F.C. Leonard, Veterinary Microbiology and Microbial Disease, second ed., Wiley-Blackwell, Iowa, 2001.

[19] A.W. Bauer, W.M.M. Kirby, J.C. Sherris, M. Turck, Antibiotic susceptibility testing by a standardized single disk method, Am. J. Clin. Pathol. 45 (1966) 493–496, https://doi.org/10.1093/ajcp/45.4_ts.493.

[20] A. S, H.P. Kavitha, Magnesium oxide nanoparticles: effective antilarvicidal and antibacterial agents, ACS Omega 8 (2023) 5225–5233, https://doi.org/10.1021/acsomega.2c01450.

[21] M.B. Coban, Hydrothermal synthesis, crystal structure, luminescent and magnetic properties of a new mononuclear Gd^{III} coordination complex, J. Mol. Struct. 1162 (2018) 109–116, https://doi.org/10.1016/j.molstruc.2018.02.089.

[22] G. Balakrishnan, R. Velavan, K. Mujasam Batoo, E.H. Raslan, Microstructure, optical and photocatalytic properties of MgO nanoparticles, Results Phys. 16 (2020) 103013, https://doi.org/10.1016/j.rinp.2020.103013.

[23] L. Rohmawati, S.N. Fathoni, W. Setyarsih, N.P. Putri, D. Darminto, Irradiation time optimization on photocatalytic activity of nanoparticles MgO from dolomite bangkalan, Trends Sci. 21 (2024) 7442, https://doi.org/10.48048/tis.2024.7442.

[24] S.M. Samatov, KhKh Turaev, B.A. Kholnazarov, A.Kh Toshkulov, D.Kh Shukurov, A.I. Kholboeva, J.T. Samariddinov, S.T. Abdurakhmonov, Synthesis hydrogels based on starch-graftacrylonitrile/bentonite, Int. J. Eng. Trends Technol. 72 (2024) 371–379, https://doi.org/10.14445/22315381/IJETT-V72I11P135.

[25] V. Onar, E. Ekdal Karali, A.S. Altowyan, H. Aydin, U.H. Kaynar, C. Gök, M. B. Coban, J. Hakami, Y. Ozcan, A. Canimoglu, N. Can, Luminescence enhancement and thermal stability of alkali co-doped Eu^{3+}:$LaMgB_5O_{10}$ phosphors, Appl. Radiat. Isot. 226 (2025) 112219, https://doi.org/10.1016/j.apradiso.2025.112219.

[26] D.A. Jabali, A.Y. Madkhli, G. Souadi, Ü.H. Kaynar, M.B. Coban, O. Madkhali, M. Ayvacikli, N. Amri, N. Can, Temperature-responsive insights: investigating Eu^{3+}

and Dy^{3+} activated yttrium calcium oxyborate phosphors for structure and luminescence, Appl. Radiat. Isot. 206 (2024) 111214, https://doi.org/10.1016/j.apradiso.2024.111214.
[27] A.S. Altowyan, M.B. Coban, U.H. Kaynar, E.A. Çin, M. Ayvacikli, J. Hakami, N. Can, Structural and photoluminescent analysis of novel Eu^{3+} and Dy^{3+} Co-doped ZnO nanoparticles by incorporation of Li^{+} and K^{+} ions, Ceram. Int. 50 (2024) 14529–14541, https://doi.org/10.1016/j.ceramint.2024.01.366.
[28] U.H. Kaynar, H. Aydin, A.S. Altowyan, J. Hakami, M.B. Coban, M. Ayvacikli, E. Ekdal Karali, A. Canimoglu, N. Can, Enhancement of luminescence and thermal stability in Eu^{3+}-doped $K_3Y(BO_2)_6$ with Li^{+} and Na^{+} co-doping, Adv. Powder Technol. 35 (2024) 104695, https://doi.org/10.1016/j.apt.2024.104695.
[29] A.S. Altowyan, U.H. Kaynar, E.A. Çin, T. Karaman, H. Aydin, M.B. Coban, J. Hakami, N. Can, Eu^{3+} and Li^{+} Co-doped $SmCa_4O(BO_3)_3$ phosphors: negative thermal quenching and photoluminescence properties, J. Alloys Compd. 1021 (2025) 179766, https://doi.org/10.1016/j.jallcom.2025.179766.
[30] A.S. Altowyan, U.H. Kaynar, H. Aydin, M.B. Coban, Z.G. Portakal, S. Akça-Özalp, J. Hakami, M. Ayvacikli, M. Topaksu, N. Can, Enhanced photoluminescence properties of Eu^{3+}/Li^{+} co-doped ZrO_2: a focus on red and far-red emissions, J. Photochem. Photobiol. Chem. 466 (2025) 116408, https://doi.org/10.1016/j.jphotochem.2025.116408.
[31] P. Kumar, D. Singh, S. Kadyan, H. Kumar, R. Kumar, Comprehensive investigation of $Y_2Si_2O_7$:Eu^{3+} nanophosphors for w-LEDs: structural, Judd-Ofelt calculation and photoluminescent characteristic with high color purity and thermal stability, Ceram. Int. 50 (2024) 34596–34608, https://doi.org/10.1016/j.ceramint.2024.06.267.
[32] K. Lenczewska, M. Ptak, V. Boiko, K. Ledwa, D. Hreniak, Energy transfer study in $GdVO_4$: Bi^{3+}, Yb^{3+} obtained by microwave-assisted hydrothermal method, J. Alloys Compd. 860 (2021) 158393, https://doi.org/10.1016/j.jallcom.2020.158393.
[33] Y.-M. Peng, Y.-K. Su, R.-Y. Yang, The charge transfer transition phenomenon and microstructure of Eu^{3+}-doped $NaCaPO_4$ phosphors sintered with NH4Cl flux via solid-state reaction, Mater. Res. Bull. 48 (2013) 1946–1951, https://doi.org/10.1016/j.materresbull.2013.01.039.
[34] A.K. Parchur, R.S. Ningthoujam, Behaviour of electric and magnetic dipole transitions of Eu3+, $^5D_0 \rightarrow {}^7F_0$ and Eu–O charge transfer band in Li^{+} co-doped YPO_4:Eu^{3+}, RSC Adv. 2 (2012) 10859 https://doi.org/10.1039/c2ra22144f.
[35] S. Kuzman, J. Periša, V. Đorđević, I. Zeković, I. Vukoje, Ž. Antić, M.D. Dramićanin, Surface plasmon enhancement of Eu^{3+} emission intensity in LaPO4/Ag nanoparticles, Materials 13 (2020) 3071, https://doi.org/10.3390/ma13143071.
[36] S. Lai, Z. Yang, J. Li, B. Shao, J. Yang, Y. Wang, J. Qiu, Z. Song, Photoluminescence enhancement of Eu^{3+} ions by Ag species in SiO_2 three-dimensionally ordered macroporous materials, J. Mater. Chem. C 3 (2015) 7699–7708, https://doi.org/10.1039/C5TC01340B.
[37] M.F. Joubert, A. Remillieux, B. Jacquier, J. Mugnier, B. Boulard, O. Perrot, C. Jacoboni, Infrared to visible conversion in rare-earth-doped planar waveguides, J. Non-Cryst. Solids 184 (1995) 341–345, https://doi.org/10.1016/0022-3093(94)00639-3.
[38] G. Blasse, Energy transfer between inequivalent Eu^{2+} ions, J. Solid State Chem. 62 (1986) 207–211, https://doi.org/10.1016/0022-4596(86)90233-1.
[39] J. Zhao, H. Gao, H. Xu, Z. Zhao, H. Bu, X. Cao, L. He, Z. Yang, J. Sun, Structure and photoluminescence of Eu^{3+} doped Sr_2InTaO_6 red phosphor with high color purity, RSC Adv. 11 (2021) 8282–8289, https://doi.org/10.1039/D1RA00165E.
[40] D.L. Dexter, J.H. Schulman, Theory of concentration quenching in inorganic phosphors, J. Chem. Phys. 22 (1954) 1063–1070, https://doi.org/10.1063/1.1740265.
[41] B.R. Judd, Optical absorption intensities of rare-earth ions, Phys. Rev. 127 (1962) 750–761, https://doi.org/10.1103/PhysRev.127.750.
[42] G.S. Ofelt, Intensities of crystal spectra of rare-earth ions, J. Chem. Phys. 37 (1962) 511–520, https://doi.org/10.1063/1.1701366.
[43] J. Jose, S. Thomas, N.D. Abraham, A.V. Lizbathu, B. Baby, P.R. Biju, C. Joseph, Judd–Ofelt analysis and luminescence studies of Eu^{3+}: $La(OH)_3$ nanophosphors synthesized via microwave enabled co-precipitation, J. Lumin. 286 (2025) 121398, https://doi.org/10.1016/j.jlumin.2025.121398.
[44] K.J. Albert, E.A. Rathnakumari, S.M.M. Kennedy, Synthesis, photoluminescent properties, and an insight into the Judd-Ofelt analysis of the $NaPbBi_{(2-x)}(PO4)_3$: xEu^{3+} orthophosphate phosphors for light applications, J. Alloys Compd. 934 (2023) 168047, https://doi.org/10.1016/j.jallcom.2022.168047.
[45] Ž. Antić, R. Krsmanović, V. Đorđević, T. Dramićanin, M.D. Dramićanin, Optical properties of Y_2O_3:Eu^{3+} red emitting phosphor obtained via spray pyrolysis, Acta Phys. Pol., A 116 (2009) 622–624, https://doi.org/10.12693/APhysPolA.116.622.
[46] V. Dimitrov, S. Sakka, Electronic oxide polarizability and optical basicity of simple oxides. I, J. Appl. Phys. 79 (1996) 1736–1740, https://doi.org/10.1063/1.360962.
[47] V. Dimitrov, S. Sakka, Linear and nonlinear optical properties of simple oxides. II, J. Appl. Phys. 79 (1996) 1741–1745, https://doi.org/10.1063/1.360963.
[48] B. Verma, R.N. Baghel, D.P. Bisen, N. Brahme, V. Jena, Judd-Ofelt analysis and luminescent characterization of Eu^{3+} activated $Li_2Zr(PO_4)_2$ phosphor, Opt. Mater. 118 (2021) 111196, https://doi.org/10.1016/j.optmat.2021.111196.
[49] K. Binnemans, Interpretation of europium(III) spectra, Coord. Chem. Rev. 295 (2015) 1–45, https://doi.org/10.1016/j.ccr.2015.02.015.
[50] M. İlhan, L.F. Güleryüz, M.İ. Katı, Study on structural, morphological, and spectral properties of $LiMPO_4$:Eu^{3+}, B^{3+} (M = Zn, Sr) phosphors and latent fingerprint applications, Mater. Sci. Eng. B 316 (2025) 118124, https://doi.org/10.1016/j.mseb.2025.118124.
[51] M. İlhan, M.İ. Katı, L.F. Güleryüz, S. Kılıç, Judd-Ofelt analysis and structural, morphological, optical characteristics of Eu^{3+} doped Ca_2GdMO_6 (M=Nb, Ta) double perovskite phosphors, J. Lumin. 286 (2025) 121361, https://doi.org/10.1016/j.jlumin.2025.121361.
[52] P. Khajuria, V.D. Sharma, I. Kumar, A. Khajuria, R. Prakash, R.J. Choudhary, Optoelectronic properties of Na_2ZrO_3:Eu^{3+} phosphor: Judd-Ofelt insights and applications in solid-state lighting and latent fingerprinting, J. Alloys Compd. 1025 (2025) 180268, https://doi.org/10.1016/j.jallcom.2025.180268.
[53] N. Vu, N.K.K. Minh, T.T.D. Hien, P.D. Roan, L.T.K. Giang, N.T. Huong, H. T. Khuyen, P.T. Lien, D.M. Tien, N.T. Kien, D.N. Nhiem, Structure, morphology, optical properties, and Judd–Ofelt analysis of $YP_{(1-x)}V_xO_4$:Eu^{3+} materials synthesized by the combustion method, Nanoscale Adv. 7 (2025) 4077–4086, https://doi.org/10.1039/D4NA01052C.
[54] S.S. Nanda, P. Nayak, S.K. Mandal, D. Jana, U.K. Goutam, S. Dash, Synthesis, Judd-Ofelt analysis and energy transfer mechanism in β-$NaYGdF_4$:Eu^{3+} microphosphors, J. Mol. Struct. 1266 (2022) 133446, https://doi.org/10.1016/j.molstruc.2022.133446.
[55] A. Ćirić, S. Stojadinović, M. Sekulić, M.D. Dramićanin, JOES: an application software for Judd-Ofelt analysis from Eu^{3+} emission spectra, J. Lumin. 205 (2019) 351–356, https://doi.org/10.1016/j.jlumin.2018.09.048.
[56] P. Kumar, D. Singh, I. Gupta, UV excitable $GdSr_2AlO_5$:Eu^{3+} red emitting nanophosphors: structure refinement, photoluminescence, Judd-Ofelt analysis and thermal stability for w-LEDs, J. Alloys Compd. 966 (2023) 171410, https://doi.org/10.1016/j.jallcom.2023.171410.
[57] V.D. Sharma, P. Khajuria, R. Prakash, R.J. Choudhary, Synthesis and luminescence properties of high-purity red-light-emitting Eu^{3+}-Doped $NaZr_2(PO_4)_3$ phosphor, J. Electron. Mater. 52 (2023) 6146–6158, https://doi.org/10.1007/s11664-023-10547-y.
[58] M. İlhan, L.F. Güleryüz, S. Gökçe, H. Demirer, Comparative luminescence and Judd–Ofelt analysis of Eu^{3+}-doped Ca_2GdVO_6 and Sr_2GdVO_6 phosphors for red-emitting applications, Mater. Sci. Eng. B 323 (2026) 118776. https://doi.org/10.1016/j.mseb.2025.118776.
[59] M. İlhan, L.F. Güleryüz, Investigation of structural, morphological and spectral characteristics of double perovskite Sr_2GdTaO_6 phosphors doped with Eu^{3+}, and co-doped Eu^{3+},B^{3+} having improved quantum efficiency, J. Mater. Sci. Mater. Electron. 35 (2024) 2163, https://doi.org/10.1007/s10854-024-13832-6.
[60] S.K. Sharma, S. Som, R. Jain, A.K. Kunti, Spectral and CIE parameters of red emitting $Gd_3Ga_5O_{12}$:Eu^{3+} phosphor, J. Lumin. 159 (2015) 317–324, https://doi.org/10.1016/j.jlumin.2014.11.010.
[61] C.S. McCamy, Correlated color temperature as an explicit function of chromaticity coordinates, Color Res. Appl. 17 (1992) 142–144, https://doi.org/10.1002/col.5080170211.
[62] Y.R. Parauha, S.J. Dhoble, Color-tunable luminescence, energy transfer behavior and I – v characteristics of Dy^{3+},Eu^{3+} co-doped $La(PO_4)$ phosphors for WLEDs and solar applications, New J. Chem. 46 (2022) 6230–6243, https://doi.org/10.1039/D2NJ00232A.
[63] C.K. Chaithra, B.R.R. Krushna, M.M. Gowri, S.C. Sharma, L. Mohapatra, R. J. Mohan, B. Subramanian, K. Manjunatha, S.Y. Wu, R. Arunakumar, H. Nagabhushana, Luminous thermal stability and versatile applications of red emitting $Ba_3Y_4O_9$: Eu3+ phosphor in W-LEDs, forensic science and security technologies, J. Lumin. 282 (2025) 121220, https://doi.org/10.1016/j.jlumin.2025.121220.
[64] V.A. Raj, V.R. Mala, S.M.M. Kennedy, H.G. Evangeline, DFT calculation, optical, photoluminescent, and radiative (Judd-Ofelt) properties of phosphate based red emitting $Na_2SrMg(PO_4)_2$:Eu^{3+} phosphor for solid state lighting, Opt. Mater. 168 (2025) 117418, https://doi.org/10.1016/j.optmat.2025.117418.
[65] X. Chen, Q. Xu, F. Hussain, C. Yang, W. Sheng, X. Luo, B. Liu, S. Sun, D. Wang, K. Song, High thermal stability and color purity of $Y_2SrAl_4SiO_{12}$:Eu^{3+} garnet-variant-structured phosphor for warm white light LED-Lamp, Crystals 12 (2022) 1382, https://doi.org/10.3390/cryst12101382.
[66] H. Yu, R. Li, J. Zhang, C. Deng, R. Cui, Multifunctional applications based on the anomalous $^5D_0 \rightarrow {}^7F_4$ transition in $SrGa_4O_7$: Eu^{3+}, Spectrochim. Acta Part A Mol. Biomol. Spectrosc. 345 (2026) 126819. https://doi.org/10.1016/j.saa.2025.126819.
[67] N. Thakan, R. Lohan, A.S. Rao, N. Deopa, Structural and luminescence attributes of Eu^{3+} ions activated Ba_2SrWO_6 phosphor for non-contact optical thermometry applications, J. Mol. Struct. 1346 (2025) 143169, https://doi.org/10.1016/j.molstruc.2025.143169.
[68] B. Shen, F. Wu, Y. Zhang, H. Xia, B. Chen, J. Hu, Multicolour emission from thermally stable Tb^{3+}/Eu^{3+} co-doped $CaLa_4Si_3O_{13}$ phosphors for single-component w-LEDs application, J. Alloys Compd. 809 (2019) 151836, https://doi.org/10.1016/j.jallcom.2019.151836.
[69] Q. Cao, L. Li, Y. Wang, W. Wang, H. Chen, Y. Pan, X. Wei, Y. Li, Synthesis and optical properties of far-red dual perovskite Sr_2InTaO_6:Mn^{4+} phosphors for indoor plant lighting LED, J. Lumin. 252 (2022) 119351, https://doi.org/10.1016/j.jlumin.2022.119351.
[70] G. Zhou, Z. Liu, M.S. Molokeev, Z. Xiao, Z. Xia, X.-M. Zhang, Manipulation of Cl/Br transmutation in zero-dimensional Mn^{2+}-based metal halides toward tunable photoluminescence and thermal quenching behaviors, J. Mater. Chem. C 9 (2021) 2047–2053, https://doi.org/10.1039/D0TC05137C.
[71] P. Linghu, X. Gong, J. Zhang, R. Cui, X. Guo, A novel red BaLaInO4:Eu^{3+} phosphor for WLEDs, J. Solid State Chem. 327 (2023) 124282, https://doi.org/10.1016/j.jssc.2023.124282.
[72] Y. Qiu, R. Cui, J. Zhang, C. Deng, A novel Eu^{3+}-doped $SrLaGaO_4$ red phosphor with high efficiency and color purity for WLED applications, J. Solid State Chem. 327 (2023) 124265, https://doi.org/10.1016/j.jssc.2023.124265.
[73] Q. Chen, X. Guo, J. Zhang, H. Xu, M. Hu, R. Cui, A novel red-emitting in the complex perovskite $Sr_3CaNb_2O_9$:Eu^{3+} phosphor with high quantum yield and

excellent thermal stability for WLEDs, J. Lumin. 258 (2023) 119813, https://doi.org/10.1016/j.jlumin.2023.119813.
[74] J. Lian, X. Miao, Y. Ran, R. Liu, X. Liu, L.-L. Zheng, R. Yu, Synthesis, characterization and application of an orange-red-emitting $InGaZnO_4$:Eu^{3+} phosphor in latent fingerprint and security ink, Solid State Sci. 157 (2024) 107702, https://doi.org/10.1016/j.solidstatesciences.2024.107702.
[75] J. Ru, F. Zeng, Y. Liu, B. Zhao, M. Li, X. Sun, F. Guo, The performance tuning of $NaCaTiTaO_6$:Dy^3+, Eu^{3+} phosphor by employing the co-doping strategy for white LED application, Opt. Mater. 144 (2023) 114345, https://doi.org/10.1016/j.optmat.2023.114345.
[76] Y. Hua, K. Zhou, X. Wang, X. Qiu, Investigations on photoluminescence properties of rare-earth ion single-doped $CaSrSb_2O_7$ phosphors, Inorg. Chem. Commun. 137 (2022) 109197, https://doi.org/10.1016/j.inoche.2022.109197.
[77] P. Bhattacharya, A. Dey, S. Neogi, An insight into the mechanism of antibacterial activity by magnesium oxide nanoparticles, J. Mater. Chem. B 9 (2021) 5329–5339, https://doi.org/10.1039/D1TB00875G.
[78] M. Rawat, P. Yadukrishnan, N. Kumar, Mechanisms of action of nanoparticles in living systems. https://doi.org/10.4018/978-1-5225-3126-5.ch014, 2018.
[79] X. Li, X. Hong, Y. Yang, J. Zhao, C.S. Diko, Y. Zhu, Enhanced antibacterial activity of acid treated MgO nanoparticles on Escherichia coli, RSC Adv. 11 (2021) 38202–38207, https://doi.org/10.1039/D1RA06221B.
[80] A. Akshaykranth, N. Jayarambabu, V.R. Tumu, R.K. Rajaboina, Comparative study on antibacterial activity of MgO nanoparticles synthesized from Lawsonia inermis leaves extract and chemical methods, J. Inorg. Organomet. Polym. Mater. 31 (2021) 2393–2400, https://doi.org/10.1007/s10904-021-01915-4.
[81] T.J. Silhavy, D. Kahne, S. Walker, The bacterial cell envelope, Cold Spring Harbor Perspect. Biol. 2 (2010) a000414, https://doi.org/10.1101/cshperspect.a000414, a000414.
[82] C. Weidenmaier, A. Peschel, Teichoic acids and related cell-wall glycopolymers in Gram-positive physiology and host interactions, Nat. Rev. Microbiol. 6 (2008) 276–287, https://doi.org/10.1038/nrmicro1861.
[83] N. Omrani, A. Nezamzadeh-Ejhieh, A novel quadripartite Cu_2O-CdS-$BiVO_4$-WO_3 visible-light driven photocatalyst: brief characterization and study the kinetic of the photodegradation and mineralization of sulfasalazine, J. Photochem. Photobiol. Chem. 400 (2020) 112726, https://doi.org/10.1016/j.jphotochem.2020.112726.
[84] R.A. Senthil, J. Theerthagiri, A. Selvi, J. Madhavan, Synthesis and characterization of low-cost g-C_3N_4/TiO_2 composite with enhanced photocatalytic performance under visible-light irradiation, Opt. Mater. 64 (2017) 533–539, https://doi.org/10.1016/j.optmat.2017.01.025.
[85] A. Toghan, A. Modwi, Boosting unprecedented indigo carmine dye photodegradation via mesoporous MgO@g-C_3N_4 nanocomposite, J. Photochem. Photobiol. Chem. 419 (2021) 113467, https://doi.org/10.1016/j.jphotochem.2021.113467.
[86] J.C. Souza, S.C.S. Lemos, M. Assis, C.H.M. Fernandes, L.K. Ribeiro, Y. Núñez-de la Rosa, M.D. Teodoro, L. Gracia, J. Andrés, L.H. Mascaro, E. Longo, Boosted photocatalytic activities of Ag_2CrO_4 through Eu^{3+} -Doping process, ACS Omega 9 (2024) 35537–35547, https://doi.org/10.1021/acsomega.4c02683.
[87] S. Ramya, S.D. Ruth Nithila, R.P. George, D.N.G. Krishna, C. Thinaharan, U. Kamachi Mudali, Antibacterial studies on Eu–Ag codoped TiO_2 surfaces, Ceram. Int. 39 (2013) 1695–1705, https://doi.org/10.1016/j.ceramint.2012.08.012.
[88] H. Madanakumara, H.S. Jayanna, C.V. Yelamaggad, S. Soundeswaran, M. Vishwas, K.S. Shamala, B.S. Surendra, N. Basavaraju, Enhanced electrochemical sensor and photodegradation of industrial wastewater by almond gum assisted synthesis of Bi_2O_3/MgO/Fe_2O_3 nanocomposites, Sens. Int. 3 (2022) 100193, https://doi.org/10.1016/j.sintl.2022.100193.
[89] R.A. Abumousa, MgO@ZrO_2@g-C_3N_4 composite for efficient photodegradation of alizarin red dye, Inorg. Chem. Commun. 155 (2023) 111086, https://doi.org/10.1016/j.inoche.2023.111086.
[90] M. Sultana, S.R. Mohapatra, M. Ahmaruzzaman, Spherical magnetic MgO-CeO_2-Fe_3O_4@JB heterojunction for enhanced photodegradation of pesticide and complex anionic dyes: understanding the degradation process and diverse water systems, Chem. Eng. J. 502 (2024) 157549, https://doi.org/10.1016/j.cej.2024.157549.
[91] Y.-X. Zhang, Y. Jia, Synthesis of MgO/TiO_2/Ag composites with good adsorption combined with photodegradation properties, Mater. Sci. Eng. B 228 (2018) 123–131, https://doi.org/10.1016/j.mseb.2017.11.024.
[92] T.M. Naren Vidaarth, S. Surendhiran, K.S.G. Jagan, S. Savitha, K.S. Balu, A. Karthik, B. Kalpana, Surface chemistry of phytochemical enriched MgO nanoparticles for antibacterial, antioxidant, and textile dye degradation applications, J. Photochem. Photobiol. Chem. 448 (2024) 115349, https://doi.org/10.1016/j.jphotochem.2023.115349.
[93] A. Ahmad, M. Khan, S. Khan, R. Luque, T.M. Almutairi, A.M. Karami, Bio-construction of MgO nanoparticles using Texas sage plant extract for catalytical degradation of methylene blue via photocatalysis, Int. J. Environ. Sci. Technol. 20 (2023) 1451–1462, https://doi.org/10.1007/s13762-022-04090-2.